

Petrogenesis of the early Cretaceous intra-plate basalts from the Western North China Craton: Implications for the origin of the metasomatized cratonic lithospheric mantle

Junjie Zhang^{1, 2, 3}, Pengyuan Guo^{1, 2*}, Pu Sun^{1, 2}, Yaoling Niu^{1, 2, 4, 5}, Yuanyuan Xiao^{1, 2}, Paulo M. Vasconcelos⁶

¹ Key Laboratory of Marine Geology and Environment, Institute of Oceanology, Chinese Academy of Sciences, Qingdao 266071, China

² Laboratory for Marine Geology, Qingdao National Laboratory for Marine Science and Technology, Qingdao 266061, China

³ University of Chinese Academy of Sciences, Beijing 100049, China

⁴ Department of Earth Sciences, Durham University, Durham DH1 3LE, UK

⁵ School of Earth Science and Resources, China University of Geosciences, Beijing 100083, China

⁶ The University of Queensland, School of Earth Sciences, Brisbane, QLD 4072, Australia

*Corresponding authors:

Dr. P.Y. Guo (guopy@qdio.ac.cn)

Current address:

Institute of Oceanology
Chinese Academy of Sciences
Nanhai Road 7
Qingdao, Shandong 266071
China

From: Dr. Pengyuan Guo
Institute of Oceanology
Chinese Academy of Sciences
Qingdao, Shandong 266071, China

To: Lithos

Date: November 03, 2020

Subject: Revised manuscript submission to Lithos for publication

Dear Editor,

Thank you very much for the constructive comments by the reviewers and yourself. We are now submitting our revised manuscript (Manuscript Number: LITHOS8954). In revision, we have considered all the comments. And we hope you and the reviewers agree that the revised version is essentially ready for publication.

Sincerely yours,

Dr. Pengyuan Guo (guopy@qdio.ac.cn)

Tel: +86-15725261166; +86-0532-82893137

Revision notes:

Thanks very much for the constructive comments by the reviewers and editor. In revision, we have considered all the comments. Furthermore, we also adjusted the text structure in section 5.3 slightly and made the language more accurate. We hope the revised version is essentially ready for publication.

Answers to reviewer:

Reviewer #1:

1. [Line 311] Generally, there are two mechanisms for continental crustal recycling into mantle, (1) lower crustal delamination; (2) continental crust subduction. The recycling of terrigenous sediments is caused by oceanic subduction.

Answer: Have changed and please see the details in the revised manuscript.

2. More statements and representative references for crustal recycling by lower crustal delamination and continental crust subduction should be given in the text.

Answer: The brief description and representative references have been added and please see the details in the revised manuscript.

We present new bulk-rock $^{40}\text{Ar}/^{39}\text{Ar}$ age, major and trace elements and Sr-Nd-Hf isotopic data on the early Cretaceous intra-plate alkali basalts from the Western North China Craton (WNCC) to study the origin of the metasomatized cratonic lithosphere mantle. The age of these basalts is ~ 116 Ma. These basalts have elevated incompatible element abundance with high $[\text{La}/\text{Sm}]_{\text{N}}$ (2.80-4.56) and enriched Sr-Nd-Hf isotopic compositions ($^{87}\text{Sr}/^{86}\text{Sr}_i = 0.7062\text{-}0.7075$, $\epsilon_{\text{Nd}}(t) = -6.0$ to -13.0 and $\epsilon_{\text{Hf}}(t) = -8.3$ to -17.4), being similar to the contemporary analogues from the Western North China Craton and Paleozoic kimberlites and mantle xenoliths. The WNCC basalts also show good correlations between $\epsilon_{\text{Nd}}(t)$ and $\epsilon_{\text{Hf}}(t)$, and high $[\text{La}/\text{Sm}]_{\text{N}}$. All these geochemical observations are consistent with the interpretation that these basalts originated from partial melting of the lithospheric mantle that experienced melt metasomatism. Two types metasomatic melts are required to explain the geochemical characteristics of these rocks. The obvious negative Nb-Ta (compared with K)-Ti and positive Ba-Pb anomalies observed in these basalts further constrain that one of the metasomatic melts was derived from the subducted terrigenous sediment. Furthermore, the overall higher P/Nd, Nb/La and Nb/Th and lower Lu/Hf of basalts in the WNCC suggest that there is also contribution of low-F melts from asthenosphere mantle. Collectively, we suggest that the formation of the metasomatized lithosphere mantle beneath the WNCC is the process of metasomatic reaction between mantle peridotite and the melts of different origin to generate metasomatic veins containing amphibole/phlogopite. Partial melting of the metasomatic lithospheric mantle at 106-120 Ma in the WNCC was considered to be induced by thermal perturbation that was ultimately related to the breakoff of the subducted oceanic slab following the closure of the Mongolia-Okhotsk ocean.

Highlight

1. We report early Cretaceous volcanic rocks in West NCC.
2. The basalts originated from partial melting of metasomatized lithospheric mantle.
- 3 Metasomatism agents were melts from asthenosphere mantle and subducted sediments.
4. The WNCC magmatism was related to slab breakoff of subducted Mongolia-Okhotsk ocean.

1 **Petrogenesis of the early Cretaceous intra-plate basalts from the**
2 **Western North China Craton: Implications for the origin of the**
3 **metasomatized cratonic lithospheric mantle**

4

5 **Junjie Zhang^{1, 2, 3}, Pengyuan Guo^{1, 2*}, Pu Sun^{1, 2}, Yaoling Niu^{1, 2, 4, 5}, Yuanyuan**
6 **Xiao^{1, 2}, Paulo M. Vasconcelos⁶**

7

8 ¹ Key Laboratory of Marine Geology and Environment, Institute of Oceanology, Chinese Academy of
9 Sciences, Qingdao 266071, China

10 ² Laboratory for Marine Geology, Qingdao National Laboratory for Marine Science and Technology,
11 Qingdao 266061, China

12 ³ University of Chinese Academy of Sciences, Beijing 100049, China

13 ⁴ Department of Earth Sciences, Durham University, Durham DH1 3LE, UK

14 ⁵ School of Earth Science and Resources, China University of Geosciences, Beijing 100083, China

15 ⁶ The University of Queensland, School of Earth Sciences, Brisbane, QLD 4072, Australia

16

17 *Corresponding authors:

18 Dr. P.Y. Guo (guopy@qdio.ac.cn)

19 Current address:

20 Institute of Oceanology

21 Chinese Academy of Sciences

22 Nanhai Road 7

23 Qingdao, Shandong 266071

24 China

25

26 **Abstract:** We present new bulk-rock $^{40}\text{Ar}/^{39}\text{Ar}$ age, major and trace elements and Sr-Nd-Hf isotopic data
27 on the early Cretaceous intra-plate alkali basalts from the Western North China Craton (WNCC) to study
28 the origin of the metasomatized cratonic lithosphere mantle. The age of these basalts is ~116 Ma. These
29 basalts have elevated incompatible element abundance with high $[\text{La}/\text{Sm}]_{\text{N}}$ (2.80-4.56) and enriched Sr-
30 Nd-Hf isotopic compositions ($^{87}\text{Sr}/^{86}\text{Sr}_i = 0.7062\text{-}0.7075$, $\epsilon_{\text{Nd}}(t) = -6.0$ to -13.0 and $\epsilon_{\text{Hf}}(t) = -8.3$ to -17.4),
31 being similar to the contemporary analogues from the Western North China Craton and Paleozoic
32 kimberlites and mantle xenoliths. The WNCC basalts also show good correlations between $\epsilon_{\text{Nd}}(t)$ and
33 $\epsilon_{\text{Hf}}(t)$, and high $[\text{La}/\text{Sm}]_{\text{N}}$. All these geochemical observations are consistent with the interpretation that
34 these basalts originated from partial melting of the lithospheric mantle that experienced melt
35 metasomatism. Two types metasomatism melts are required to explain the geochemical characteristics
36 of these rocks. The obvious negative Nb-Ta (compared with K)-Ti and positive Ba-Pb anomalies
37 observed in these basalts further constrain that one of the metasomatic melts was derived from the
38 subducted terrigenous sediment. Furthermore, the overall higher P/Nd, Nb/La and Nb/Th and lower
39 Lu/Hf of basalts in the WNCC suggest that there is also contribution of low-F melts from asthenosphere
40 mantle. Collectively, we suggest that the formation of the metasomatized lithosphere mantle beneath the
41 WNCC is the process of metasomatic reaction between mantle peridotite and the melts of different origin
42 to generate metasomatic veins containing amphibole/phlogopite. Partial melting of the metasomatic
43 lithospheric mantle at 106-120 Ma in the WNCC was considered to be induced by thermal perturbation
44 that was ultimately related to the breakoff of the subducted oceanic slab following the closure of the
45 Mongolia-Okhotsk ocean.

46 **Keywords:** Western North China Craton, K-rich basalt, mantle metasomatism, craton metasomatized
47 lithosphere, subducted terrigenous sediments, Low-F melt

48 1. Introduction

49 Cratonic lithospheric mantle is physically thick, cold, buoyant and rigid and geochemically
50 depleted in incompatible element with high MgO and low FeO, which is thought to be the residue of the
51 upper mantle after high extent of melt extraction in early history of the earth (e.g., Abbot et al., 1997;
52 Jordan, 1988; Ringwood, 1975). For this reason, the overlying continental crust can survive for a long
53 time. However, the processes of lateral subduction (e.g., Hawkesworth, 1993) and vertical upwelling of
54 melts/fluids from the asthenospheric mantle (e.g., Niu, 2005, 2014) could potentially change the
55 mineralogy and geochemistry of the cratonic lithosphere mantle, resulting in varying extents of
56 lithosphere modification/re-fertilization and increasing the susceptibility of the craton
57 destruction/lithosphere thinning. Therefore, the melts or xenoliths derived from such ancient
58 metasomatized cratonic lithosphere mantle, for example, the North China Craton (NCC), would contain
59 important information on the cratonic lithosphere re-fertilization history.

60 Previous studies, mostly based on >110 Ma mafic igneous rocks in the Eastern North China
61 Craton (ENCC), showed that the partial melts derived from the metasomatized NCC lithospheric mantle
62 share the similar continental crust-like signatures of being enriched in large ion lithosphere elements
63 (LILE; e.g., Rb, Ba, K), depleted in high field strength elements (HFSE; e.g., Nb, Ta, Ti) and with
64 enriched Sr-Nd-Hf isotope compositions (radiogenic Sr and unradiogenic Nd-Hf) (e.g., Dai et al., 2016;
65 Liu et al., 2008; Meng et al., 2015), implying that the whole NCC lithospheric mantle experienced re-
66 fertilization before partial melting. Formation of the enriched lithosphere mantle of NCC has been
67 ascribed to: (1) the delamination of the lower continental crust (e.g., Gao et al., 2004, 2008; Liu et al.,
68 2008); (2) the subduction of continental crust of South China Block (e.g., Dai et al., 2016; Yang et al.,
69 2012; Zhang et al., 2002; Zhao et al., 2018); (3) the subduction of the Paleo-Pacific plate (e.g., Ma et al.,

70 2014). The “delamination of lower crust” model deciphers the scenario that the lithosphere mantle was
71 enriched/metasomatized by the melts derived from foundered lower crust (Gao et al., 2004, 2008; Liu et
72 al., 2008). While this model is attractive, it is physically not straightforward how the lower continental
73 crust of the NCC together with buoyant lithospheric mantle foundered into the asthenosphere mantle in
74 scale of the whole North China (Niu, 2014). Furthermore, the thickening of the lower crust is the
75 prerequisite for the crust delamination. But except for some areas (e.g., Xuhuai), there is no enough
76 evidence to show that this process occurred in the whole North China Craton (Wu et al., 2008 and
77 references therein). The “continent-continent subduction/collision” model means the lithosphere mantle
78 enriched through interaction with melt generated from melting of the subducted crust of South China
79 Block (Dai et al., 2016; Yang et al., 2012; Zhang et al., 2002; Zhao et al., 2018). This model cannot
80 explain the origin of the enriched lithospheric mantle beneath the north margin and interior of the NCC,
81 but only works restricted to the areas close to the Dabie–Sulu Orogenic Belt. Some studies suggest the
82 lithosphere mantle was modified by subduction-related fluids from Paleo-Pacific plate (e.g., Ma et al.,
83 2014). Similarly, the subduction of the Paleo-Pacific plate modal cannot explain the origin of the enriched
84 lithospheric mantle beneath the area far from the Pacific subduction zone, for example, the Western North
85 China Craton (WNCC).

86 There is growing evidence that the lithosphere under WNCC has also been thinning in the
87 Mesozoic (Chen et al., 2009; Guo et al., 2014) as evidenced by the widespread late Cretaceous volcanic
88 rocks along north margin of WNCC (Fig. 1a; Guo et al., 2014, 2018; He et al., 2013; Zhang, 2013; Zhong
89 et al., 2014, 2015; Zou et al., 2008). These early Cretaceous basalts have high incompatible element
90 abundances and highly enriched Sr-Nd-Hf isotopic compositions (e.g., Guo et al., 2014, 2018; Zhong et
91 al., 2014, 2015), implying they also originated from an ancient metasomatized lithosphere mantle (Guo

92 et al., 2014, 2018). However, the mechanism of the enriched mantle formation was unclear in details.
93 The study of lithosphere mantle enrichment beneath northern margin of WNCC could help us to
94 understand the mantle re-fertilization beneath the area far from Dabie–Sulu Orogenic Belt and Pacific
95 subduction zone and have a significant meaning in the exploration of the evolution of whole NCC.

96 Here we present new bulk-rock $^{40}\text{Ar}/^{39}\text{Ar}$ dating, major element, trace element and Sr-Nd-Hf
97 isotopic data on the early Cretaceous basalts from Wulate Zhongqi and Heishitougou, Western North
98 China Craton (WNCC; Fig. 1) to study the origin of the metasomatized lithospheric mantle beneath
99 WNCC. The data suggest that the enriched lithospheric mantle beneath the WNCC was formed through
100 metasomatism by silicate melts derived from terrigenous sediments and low-F melts from asthenosphere
101 mantle. These processes could lead to the formation of metasomatic dikes/veins containing
102 amphibolite/phlogopite. Integrated with the regional geology, we suggest that the sediments were
103 recycled into the mantle depth together with the subducted Paleo-Asia ocean slab in early Paleozoic,
104 while subsequent melting of the metasomatized lithospheric mantle materials in early Cretaceous
105 produced the WNCC intra-plate alkali basalts.

106 2. Geological setting and samples

107 The North China Craton is one of the oldest cratons on the earth with the history in excess of 3.8
108 Gyrs (e.g., Liu et al., 1992). It is bounded by the Central Asian Orogenic Belt (CAOB) to the north and
109 the Qinling-Dabie-Sulu high-ultrahigh pressure metamorphic belt to the south (Fig. 1a). It can be divided
110 into Eastern North China Craton (ENCC) and Western North China Craton (WNCC) based on the studies
111 of the basement rocks (Fig. 1a; e.g., Zhao et al., 2001). The WNCC is further divided into the Yinshan
112 block in the north and the Ordos block in the south by the nearly E-W trending, ca. 2.0 to 1.9 Ga
113 Khondalite Belt (Zhao et al., 2005). After the amalgamation of the eastern and western blocks, the North

114 China Craton remained tectono-thermally quiescent until the Mesozoic. Previous studies showed that the
115 ENCC experienced extensive destruction/lithosphere thinning in the Mesozoic ($> \sim 110$ Ma) (Niu, 2005,
116 2014; Zhu et al., 2011), while the lithosphere thinning in the WNCC was limited in the northern margin
117 (Chen et al., 2009; Guo et al., 2014).

118 The northern margin of the WNCC was an active continental margin during Paleozoic to Early
119 Triassic with the Paleo-Asian slab subducting southward (Li, 2006; Xiao et al., 2003; Zhang et al., 2009).
120 The Paleo-Asian ocean closed in early Triassic when the North China Craton collided with the southern
121 Mongolian composite terrane along the Solonker Suture (SLS; Wilde, 2015). Following the closure of
122 the Paleo-Asian ocean, the northern margin of the NCC became active continental margin again with the
123 Mongolia-Okhotsk Ocean subducting southward. The Mongolia-Okhotsk Ocean was ultimately closed
124 in Jurassic to the earliest Cretaceous (Donskaya et al., 2013; Tomurtogoo et al., 2005), and the region
125 came into intra-plate tectonic setting in early Cretaceous. So far, only several outcrops of Early
126 Cretaceous volcanic rocks have been reported in the WNCC, i.e., Siziwang Qi, Wuchuan Basin, Guyang
127 Basin, Wulate Houqi and Suhongtu, dominated by mafic-intermediate compositions with minor felsic
128 volcanic assemblages (Fig. 1a; Guo et al., 2014, 2018; He et al., 2013; Zhang, 2013; Zhong et al., 2014,
129 2015; Zou et al., 2008). These volcanic rocks were erupted during 135~105 Ma and are spatially
130 distributed along the northern margin of the WNCC (Table 1 and Fig.1a), forming an E-W trending
131 volcanic rock belt.

132 Wulate Zhongqi is a newly identified Mesozoic volcanism outcrop that is located on the north
133 margin of the WNCC (Fig. 1). These basalts, erupted on the Cretaceous red sedimental layer (Fig. 2a),
134 covers a large area of ~ 240 km² (Fig. 1b). Heishitougou is located ~ 150 km south of the Wulate Zhongqi
135 in Khondalite Belt (Fig. 1). Heishitougou volcanic rocks are covered under the Quaternary sediments

136 with very limited outcrops of 2-3 meters thick (Fig. 2b) and their eruption age is 126.2 Ma (Zou et al.,
137 2008). The samples in this study include Wulate Zhongqi basalts and andesitic basalts and Heishitougou
138 basalts. Most basalt and andesitic basalt samples are massive with intergranular texture, being made up
139 of microlites of plagioclase, olivine, clinopyroxene and magnetite (Fig. 2c, d, f). Several Wulate Zhongqi
140 samples have porphyritic texture with olivine (~5-10%) and plagioclase (~5%) as phenocrysts, and most
141 of olivine phenocrysts were altered into iddingsite (Fig. 2e). Their groundmass, with intergranular
142 texture, is made up of microlites of plagioclase, clinopyroxene and olivine (Fig. 2e).

143 3. Sample preparation and analytical procedure

144 3.1 ^{40}Ar - ^{39}Ar Geochronology

145 We selected the freshest basaltic sample (ZQ14-47; Fig. 2f) for ^{40}Ar - ^{39}Ar dating. The sample grains
146 were irradiated for 14 hours in the Cadmium-lined B-1 CLICIT facility, a TRIGA-type reactor, in Oregon
147 State University, USA. After a decay period of irradiation, samples were analysed by laser $^{40}\text{Ar}/^{39}\text{Ar}$
148 heating following procedures detailed in Vasconcelos et al. (2002). Before analysis, the rock grains and
149 fluence monitors were baked-out under vacuum at ~200 °C for ~12 hours. The sample was heated
150 incrementally with a continuous-wave Verdi Diode laser (532 nm) with a 2 mm wide defocused beam.
151 The fraction of gas released was cleaned through a cryocooled cold-trap (T = -125 °C) and two C-50
152 SAES Zr-V-Fe getters and analysed for Ar isotopes in a MAP215-50 mass spectrometer equipped with
153 a third C-50 SAES Zr-V-Fe getter. Analytical procedures followed are described in Deino and Potts
154 (1990) and Vasconcelos et al. (2002). A $^{40}\text{Ar}/^{36}\text{Ar}$ value of 298.56 ± 0.31 for atmospheric argon was used
155 for the calculation of the mass spectrometer discrimination (Renne et al., 2009). The irradiation
156 correction factor (J) for each Al-disk were determined by the laser total fusion analyses of 15 individual
157 aliquots of neutron fluence monitor.

158 3.2 Geochemistry

159 Eighteen samples were chosen for geochemical analyses. We removed weathered surfaces, pen
160 marks and saw marks first. All samples were crushed into grains of ~0.5-1.0 mm size to painstakingly
161 remove phenocrysts under a binocular. The sample grains were then ultrasonically-cleaned with Milli-Q
162 water and dried in a clean environment before analyses.

163 All the bulk-rock geochemical analyses were done at the Laboratory of Ocean Lithosphere and
164 Mantle Geodynamic, Institute of Oceanology, Chinese Academy of Sciences. Major elements were
165 analyzed using an Agilent 5100 inductively coupled plasma-optical emission spectroscopy (ICP-OES)
166 following Kong et al. (2019). After dried at 105 °C for ~2 hours in the oven, about ~50 mg rock powders
167 were weighted in platinum crucibles together with ~250 mg lithium metaborate. The platinum crucibles
168 were heated in the muffle furnace at 1050 °C for 2 hours until the mixture completely molten. The crucible
169 was further heated over a Bunsen burner (Dragon series) at 1000 °C and stirred to ensure all sample
170 materials forming a single coherent melt drop that was finally poured/quenched and resolved in 5%
171 HNO₃ at room temperature. USGS standards materials BCR-2 and AGV-2 were used to monitor the
172 analytical accuracy and precision. For loss on ignition (LOI) analysis, ~500 mg samples were weighed
173 and heated in a muffle furnace at 1000 °C for 30 min, cooled in a desiccator, and then weighed again to
174 calculate the weight loss as the LOI (see [Supplementary Table 1](#)).

175 Trace elements were analyzed using an Agilent-7900 inductively coupled plasma mass
176 spectrometer (ICP-MS) following Chen et al. (2017). About 50 mg rock powders were dissolved with
177 distilled HNO₃+ HCl+ HF in a high-pressure jacket equipped Teflon beaker at 190 °C for 15 hours. The
178 sample solutions are then evaporated to incipient dryness at 100 °C, refluxed with 2 ml of concentrated
179 HNO₃ before being heated again to incipient dryness to remove all the residual HF, and then re-dissolved

180 with distilled 20% HNO₃ for 2 hours till complete digestion/dissolution. USGS standards materials BCR-
181 2 and AGV-2 were used to monitor the analytical accuracy and precision (see [Supplementary Table 1](#)).

182 The Sr-Nd-Hf isotope ratios were measured using a Nu Plasma II Multi-Collector Inductively
183 Coupled Plasma Mass Spectrometer (MC ICP-MS) following the procedures of Sun et al. (2019). The
184 sample dissolving process was similar to that for trace elements analysis, and the final solution was re-
185 dissolved in 2 ml 3N HNO₃. The final sample solution was first loaded onto Sr-spec resin columns to
186 separate Sr with the eluted sample solution collected and then loaded onto AG 50W-X8 resin columns
187 to separate REE. The eluted sample solution from AG 50W-X8 resin columns was collected and then
188 loaded onto Ln-spec resin columns to collect Hf. The separated REE solution was dried and re-dissolved
189 with 0.25 N HCl before being loaded onto Ln-spec resin columns to collect Nd. The measured ⁸⁷Sr/⁸⁶Sr,
190 ¹⁴³Nd/¹⁴⁴Nd, and ¹⁷⁶Hf/¹⁷⁷Hf isotope ratios were normalized for instrumental mass fraction using the
191 exponential law to ⁸⁶Sr/⁸⁸Sr = 0.1194, ¹⁴⁶Nd/¹⁴⁴Nd = 0.7219 and ¹⁷⁹Hf/¹⁷⁷Hf = 0.7325, respectively.
192 Standards of NBS-987, JNdi-1 and Alfa Hf were analyzed every three to five samples to monitor the
193 instrument drift for Sr, Nd and Hf isotopes, respectively. Repeated analysis for NBS-987 gave an average
194 ⁸⁷Sr/⁸⁶Sr = 0.710251 ± 0.000020 (n=8, 2σ), for JNdi-1 gave an average ¹⁴³Nd/¹⁴⁴Nd = 0.512111 ±
195 0.000003, (n=6, 2σ), and for Alfa Hf gave an average ¹⁷⁶Hf/¹⁷⁷Hf = 0.282196 ± 0.000007 (n=8, 2σ). The
196 analysis results of USGS reference materials AGV-2, BCR-2 and BHVO-2 run with our samples are
197 given in [Table 2](#), which are all consistent with the reported reference values (GeoREM,
198 <http://georem.mpch-mainz.gwdg.de/>).

199 4. Results

200 4.1 ⁴⁰Ar-³⁹Ar geochronological data

201 The ⁴⁰Ar-³⁹Ar age data for sample ZQ14-47 from Wulate Zhongqi is reported in [Supplementary](#)

202 Table 2 and shown in Fig. 3. The sample was analysed twice, and the two incremental heating spectra of
203 sample ZQ14-47 define similar plateau-like segments, containing ~40 and 50% of the total ^{39}Ar released,
204 and these plateau-like segments yield compatible ages of 119.65 ± 0.40 and 119.54 ± 0.53 Ma (Fig. 3a).
205 An integrated apparent age obtained by combining the results from all steps analysed is also shown (Fig.
206 3b). Inverse isochron was gotten by plotting all results on a $^{39}\text{Ar}/^{40}\text{Ar}$ vs. $^{36}\text{Ar}/^{40}\text{Ar}$ diagram and the
207 inverse age was calculated from the $^{39}\text{Ar}/^{40}\text{Ar}$ intercept of isochron on the diagram. However, the inverse
208 isochron suggests significant excess argon in the sample ($^{40}\text{Ar}/^{36}\text{Ar}$ intercept = 857 ± 72). In this case,
209 the inverse isochron is more reliable here and the calculated inverse isochron age is 116.35 ± 0.75 Ma.
210 Therefore, the age of these basalts is ~116 Ma.

211 4.2 Geochemical data

212 Major and trace element data on our WNCC basalt samples are given in Supplementary Table 1.
213 These samples have high alkali content ($\text{Na}_2\text{O} + \text{K}_2\text{O} = 4.81\text{-}7.78$ wt.%), and they are trachybasalts,
214 basaltic trachyte-andesite and trachyandesite according to Le Bas et al. (1986) (Fig. S1a) and belong to
215 shoshonite and high-K series according to Le Maitre et al. (1989) (Fig. S1b). For simplicity, these
216 samples are hereafter referred to as basalt. Volcanic rocks from Wulate Zhongqi display a relative larger
217 compositional variation (Fig. 4 & S1). Samples from Wulate Zhongqi show increasing SiO_2 , Al_2O_3 and
218 TiO_2 and decreasing $^{\text{T}}\text{Fe}_2\text{O}_3$, $\text{CaO}/\text{Al}_2\text{O}_3$, Cr and Ni with decreasing MgO (Fig. 4). The Heishitougou
219 samples have a uniform composition with higher TiO_2 , $^{\text{T}}\text{Fe}_2\text{O}_3$, and lower SiO_2 at a given MgO when
220 compared with the Wulate Zhongqi samples (Fig. 4).

221 In chondrite-normalized rare earth element (REE) diagram (Fig. 5a), the WNCC samples show
222 consistent enrichment in light rare earth elements (LREEs) and depletion in heavy rare earth elements
223 (HREEs) ($[\text{La}/\text{Sm}]_{\text{N}} = 2.80\text{-}4.56$) without obvious Eu negative anomaly, being similar to the >110 Ma

224 basaltic rocks in ENCC (Dai et al., 2016; Liu et al., 2008). In primitive mantle normalized multi-element
225 spidergram (Fig. 5b), these samples display positive Ba and Pb anomalies and negative Ti anomalies.
226 Different from the analogues in the ENCC (Dai et al., 2016; Liu et al., 2008), basalts from WNCC have
227 higher Nb-Ta-Ti abundances and thus show less obvious Nb-Ta trough, implying somewhat different
228 mantle source or source history.

229 Bulk-rock Sr, Nd and Hf isotopic data of our WNCC samples are given in Table 2. The initial Sr-
230 Nd-Hf isotope ratios were calculated using the age of 116.35 Ma (this study) and 126.2 Ma (Zou et al.,
231 2008) for samples from Wulate Zhongqi and Heishitougou, respectively. Generally, these samples show
232 enriched isotopic compositions with a large range of $^{87}\text{Sr}/^{86}\text{Sr}_i = 0.7062\text{-}0.7075$, $\epsilon_{\text{Nd}}(t) = -6.0$ to -13.0 and
233 $\epsilon_{\text{Hf}}(t) = -8.3$ to -17.4 , plotting in the field defined by the >110 Ma basaltic rocks from the ENCC in both
234 Sr-Nd and Hf-Nd isotopes spaces (Fig. 6).

235 5. Discussions

236 5.1 Evaluation of post-magmatic processes

237 The samples in this study have been altered to some extent based on the petrographic observation
238 (Fig. 2c-e) and high LOI ($>2.5\%$) in 8 samples (Supplementary Table 1). However, our samples show
239 good correlations between “alteration immobile” elements (e.g., Zr) and most other elements (e.g., Ba,
240 Pb, La, Hf) (Fig. S2), implying that most elements are not influenced by such slight alteration and only
241 Rb was affected in some samples. For these reasons, the following discussion will not involve the
242 elements affected by alteration (e.g., Rb), but use those more immobile elements such as Th, REE, HFSE.

243 The Wulate Zhongqi samples have relatively large SiO_2 variation (50.71-57.32 wt.%) with low MgO
244 (1.58-5.45 wt.%), Ni (16-55 ppm) and Cr (26-102 ppm) concentration, indicating their evolved nature
245 from mantle-derived parental melts through fractional crystallization. The correlated variations between

246 ${}^T\text{Fe}_2\text{O}_3$, $\text{CaO}/\text{Al}_2\text{O}_3$, Ni, Cr and MgO (Fig. 4) indicate the olivine and clinopyroxene as the dominant
247 fractional crystallization phases, being consistent with the petrographic observation. Furthermore, the
248 negative correlation between Al_2O_3 and MgO (Fig. 4c) and no obvious Eu negative anomalies (Fig. 5a)
249 suggest that plagioclase was not the dominant fractional crystallization phase.

250 Crustal contamination is inevitable for mantle-derived melts during their ascent through the thick
251 continental crust. Thus, it is necessary to evaluate the effect of crustal contamination before using the
252 geochemical data to discuss their source characters and mantle melting processes. The continental crust
253 is characterized by elevated abundances of SiO_2 and LILEs and depletion in HFSEs with low ${}^{143}\text{Nd}/{}^{144}\text{Nd}$
254 (Gao et al., 1998; Liu et al., 2004). If a significant volume of crustal materials was involved, there must
255 be an obvious positive relationship between SiO_2/MgO , Nb/La and $\epsilon_{\text{Hf}}(t)$ (or $\epsilon_{\text{Nd}}(t)$). The rough
256 correlations between $\epsilon_{\text{Hf}}(t)$ and these element ratios are found in four samples (ZQ14-09, ZQ14-26,
257 ZQ14-52, ZQ19-08), indicating that they had undergone various levels of crustal assimilation (Fig. 7).
258 However, for most samples, crustal contamination is limited (Fig. 7). Thus, the characteristics of these
259 samples, excluding ZQ14-09, ZQ14-26, ZQ14-52 and ZQ19-08, could reflect those of the magma source,
260 and the four samples potentially contaminated by the crustal materials would not be covered in the
261 following discussion.

262 **5.2 Melt metasomatized lithospheric mantle source of the WNCC basalts**

263 Previous studies explain the widespread >110 Ma intra-plate alkali basalt with high ${}^{87}\text{Sr}/{}^{86}\text{Sr}$, low
264 ${}^{143}\text{Nd}/{}^{144}\text{Nd}$ and low ${}^{176}\text{Hf}/{}^{177}\text{Hf}$ in the ENCC (Fig. 6; Dai et al., 2016; Meng et al., 2015) as the partial
265 melts of the metasomatized cratonic lithosphere (e.g., Meng et al., 2015; Niu, 2005, 2014). This is easily
266 understood. As the cratonic lithospheric mantle is isolated from the underlying convective mantle, it
267 tends to inherit the enriched isotopic compositions of metasomatic agents once the mantle was

268 metasomatized by isotopically enriched melts or tends to accumulate radiogenic isotopes with time if the
269 mantle was metasomatized by melts with high parent/daughter ratios. The basalts from the Wulate
270 Zhongqi and Heishitougou show significantly radiogenic Sr and un-radiogenic Nd-Hf isotopic
271 compositions, being distinctly different from the asthenospheric mantle derived mid-ocean ridge basalts
272 (MORB) but plotted in the region defined by the >110 Ma basalts from ENCC and basalts with similar
273 age from WNCC in Sr-Nd and Nd-Hf isotopes spaces (Fig. 6). This implies that basalts from Wulate
274 Zhongqi and Heishitougou shared similar origin from partial melting of the lithospheric mantle with
275 these ENCC and WNCC basalts. Importantly, in Sr-Nd isotope space, these basalts also plot in the field
276 of NCC ancient lithosphere mantle represented by Paleozoic kimberlites and mantle xenoliths from NCC
277 (Fig. 6a), providing evidence that the source of these basalts is lithosphere mantle.

278 Theoretically, the craton lithospheric mantle is the partial melting residues, refractory and highly
279 depleted in incompatible elements (Abbot et al., 1997; Jordan, 1988; Ringwood, 1975). However, this is
280 inconsistent with the basic observation that the occurrence of large scale of the Mesozoic volcanism (Zhu
281 et al., 2011) and incompatible elements highly enriched magmas derived from such a craton lithospheric
282 mantle (e.g., Dai et al., 2016; Liu et al., 2008). This implies that the enrichment or re-fertilization
283 process/processes occurred at the mantle lithosphere before its melting. The WNCC basalts display
284 remarkably enrichment in incompatible elements with high $[La/Sm]_N = 2.80-4.56$ (Fig. 5), indicating that
285 their mantle source was enriched by melts. Specifically, the significantly correlated $\epsilon_{Nd}(t)$ with $\epsilon_{Hf}(t)$ ($R=$
286 0.968) in these samples (excluding the sample ZQ14-29) is consistent with that the mantle source isotopic
287 variation is largely controlled by simple magmatic processes. All these geochemical observations imply
288 that the mantle source of the WNCC basalts was the craton lithospheric mantle that was metasomatized
289 by melts.

290 5.3 The origin of the metasomatic melt and the formation of enriched lithosphere mantle

291 WNCC basalts display obviously different incompatible element distribution pattern from
292 present-day average OIB with negative Nb-Ta (compared with K) -Ti and positive Ba-Pb anomalies (Fig.
293 5). Several processes can be responsible for the negative Nb-Ta (compared with K) and Ti anomalies in
294 these samples (Fig. 5): (1) the involvement of the continental crust materials during the magma ascent;
295 (2) Ti-rich mineral (e.g., amphibole, rutile) crystallization during the magma evolution or being as a
296 residual phase in the source region (e.g., Tiepolo et al., 2001; Xiong et al., 2005); (3) Contribution of
297 crustal component in the mantle source (e.g., Cheng et al., 2018; Dai et al., 2016; Liu et al., 2008). First,
298 as discussed above, continental crustal contamination was negligible in the petrogenesis of our samples.
299 Second, TiO₂ increases with the decreasing MgO in our samples (Fig. 4d), arguing against the Ti-bearing
300 minerals crystal fractionation. Furthermore, the fractional crystallization of Ti-bearing minerals or their
301 being as a residual phase in the source region could not produce the Pb anomaly as observed in our
302 samples (Fig. 5b). Therefore, the involvement of crustal materials was the most probable cause to the
303 Nb-Ta-Ti and positive Pb-Ba anomalies in the mantle source of these basalts (Fig. 5b).

304 Three mechanisms have been proposed to produce continental crustal material recycling into
305 mantle: (1) lower crustal delamination (e.g., Gao et al., 2004, 2008; Liu et al., 2008); (2) continental crust
306 subduction (e.g., Dai et al., 2016; Yang et al., 2012; Zhang et al., 2002; Zhao et al., 2018); (3) sediments
307 recycling by oceanic subduction (e.g., Cheng et al., 2018; Sun et al., 2019). Zhang et al. (2012) suggested
308 that the lithosphere mantle beneath WNCC was not newly-accreted in the Phanerozoic but was
309 transformed from the Archean-Proterozoic lithospheric mantle. Considering the existence of ancient
310 lithospheric relicts in the lithosphere mantle beneath the WNCC, the possibility of lower crust with
311 lithosphere mantle foundering (delamination) into the denser asthenosphere could be excluded.

312 Furthermore, there is no evidence of continental crust subduction in the study area just as the case of
313 South China block subduction underneath the southern margin of the NCC. We therefore suggest the
314 continental crust materials presenting in the mantle source region was most likely originated from
315 subducted sediments. This inference is also consistent with the research of Tertiary basalts-hosted
316 xenoliths from north margin NCC (Wang et al., 2019). Subduction sediments consist of terrigenous
317 sediments and pelagic sediments. Considering that most trace elements (e.g., alkali elements, HFSEs,
318 REEs) of subduction sediments are mainly linked to terrigenous sediments (Plank and Langmuir, 1998),
319 we suggest the crust-like geochemical characters of basalts in this study are the results of involvement
320 of terrigenous sediments in the mantle source. Because the subducted terrigenous sediments is
321 characterized by depletion in HFSEs and P and enriched Sr-Nd-Hf isotope composition (Plank and
322 Langmuir, 1998), the contribution of terrigenous sediment material into the mantle source would
323 decrease P/Nd, Nb/La, $\epsilon_{Nd}(t)$ and $\epsilon_{Hf}(t)$ in the erupting magma. This is indeed the case for the WNCC
324 basalts, with both $\epsilon_{Nd}(t)$ and $\epsilon_{Hf}(t)$ showing positive correlation with P/Nd and Nb/La (Fig. 8a-d).
325 Therefore, the silica-rich melts derived from subducted terrigenous sediments is an important
326 metasomatism agent beneath WNCC.

327 However, the mantle source only metasomatized by silica-rich melts derived from subducted
328 sediment is not consistent with the geochemical trends of WNCC basalts (Fig. 8), which requires another
329 enriched component in the mantle source. This component must have higher Nb/La and P/Nd, lower
330 Sm/Nd and Lu/Hf than N-MORB and moderately low $\epsilon_{Nd}(t)$ and $\epsilon_{Hf}(t)$ (Fig. 8), which implies that this
331 component is characterized by enrichment of incompatible elements and more enrichment in the
332 progressively more incompatible elements. The most likely candidate for this enriched component is the
333 low mass fraction (low-F) melts (Niu and O'Hara, 2003; Niu et al., 2012). Niu and coauthors suggest

334 such low-F melts may develop within asthenosphere/LVZ and is enriched in volatiles, alkalis and
335 incompatible elements, and it will develop low $\epsilon_{Nd}(t)$ and $\epsilon_{Hf}(t)$ after long-term accumulation of
336 radioisotopes, because of its low Sm/Nd and Lu/Hf (Niu and O'Hara, 2003; Niu et al., 2012). They also
337 proposed that OIB was originated from such low-F melts metasomatized mantle (Niu and O'Hara, 2003;
338 Niu et al., 2012). The occurrence of the Early Cretaceous basalts with OIB-like trace elements patterns
339 from Suhongtu and Siziwangqi in the WNCC (Guo et al., 2014; Hui et al., 2020) suggests that low-F
340 melts metasomatism process is common in the lithosphere mantle beneath the region. Note that the
341 WNCC lavas display a contrasting difference from the contemporary analogues in ENCC with obvious
342 Th-U negative anomalies relative to Nb-Ta (Fig. 5b). We explain this observation as the result of the
343 involvement of phlogopite/amphibole metasomes during magma event that produce WNCC lavas. This
344 is because reaction between low-F melts from asthenosphere and Si-poor peridotites could produce
345 phlogopite/amphibole metasomes (Niu, 2008; Pilet et al., 2011; Soder et al., 2016) and partial melts
346 derived from the phlogopite/amphibole -bearing mantle could inherit their mantle source low Th-U and
347 elevated Nb-Ta characters (Pilet et al., 2008).

348 To illustrate the two metasomatic melts roles in the formation of the metasomatic lithospheric
349 mantle source of the WNCC Mesozoic basalts, we approximate basalts from Siziwangqi as the result of
350 partial melts derived from low-F melts metasomatized mantle (Guo et al., 2014) and choose global
351 subducted sediments (GLOSS, Plank and Langmuir, 1998) as the end-members of subducted terrigenous
352 sediments to model its contribution. The modeling result shows that ~40% terrigenous sediments are
353 required to mix with the Siziwangqi highly enriched basaltic melts to produce the Wulate Zhongqi and
354 Heishitougou lavas (Fig. 9). Not that the modelling result is not unique, which depends on end-members
355 and parameters we chose. However, what we emphasis here is that there are two different metasomatized

356 agents in the WNCC basalts mantle source.

357 In conclusion, despite the possible varied compositions of the initial metasomatism melts (derived
358 from subducted sediments or asthenosphere) and the complex reaction between the melts and the
359 peridotite matrix, the ultimate result of such a metasomatism is the formation of the metasomes
360 characterized by an assemblage of hydrous and anhydrous metasomatic minerals such as pyroxene,
361 amphibole and/or phlogopite (Förster et al., 2019; Niu, 2008; Pilet et al., 2011; Sekine and Wyllie, 1983;
362 Soder et al., 2016; Wyllie and Sekine, 1982). Partial melting of such metasomatized mantle produced K-
363 enriched and shoshonitic WNCC basalts, and these basalts inherited the geochemical characters of
364 terrigenous sediments and low-F melts from asthenosphere with enrichment in incompatible elements,
365 obvious Nb-Ta (compared with K)-Ti negative anomalies, Ba-Pb positive anomalies and Th-U trough
366 (Fig. 5b).

367 **5.4 A petrogenetic model for the generation of widespread WNCC basalts**

368 Because the study area is located at the northern margin of the NCC, the first and foremost tectonic
369 background related to these magmatism activities is the closure of the Paleo-Asian ocean. However, the
370 Paleo-Asian ocean was closed in late Permian to early Triassic (Li, 2006; Xiao et al., 2003; Zhang et al.,
371 2009). The temporal span from such an event to the early Cretaceous magmatism is at least ~100 Myrs,
372 which makes it impossible to be related with each other. In addition, as there is no known regional domal
373 uplift nor the presence of volumetrically significant “large igneous province”, the WNCC volcanisms are
374 unlikely to have been caused by a hotspot or mantle plume. Third, the addition of fluids, released from
375 the speculated Paleo-Pacific slabs lying in the transition zone, to the ancient craton lithosphere could
376 well explain the >110 Ma basaltic magmatism in the ENCC (Niu, 2005, 2014). But this mechanism may
377 not apply here because the WNCC is too far (~1500 km) away from the speculated western pacific

378 subduction zone. Thus, other mechanism is required to explain the petrogenesis of these intra-plate
379 basalts.

380 Previous studies demonstrate that extensional basins (e.g., Graham et al., 2001) and metamorphic
381 core complexes (e.g., Davis et al., 2002) of early Cretaceous ages are widespread in the northern margin
382 of the WNCC, suggesting an extensional setting at that time in the region. Some authors explained such
383 an extension to be related with the breakoff of subducted oceanic slab after the closure of Mongolia-
384 Okhotsk Ocean in the Middle Jurassic (Li et al., 2018; Ouyang et al., 2015). Our contemporary basaltic
385 volcanism in WNCC supports this model. We also suggest that the early Cretaceous basaltic volcanism
386 in the WNCC in this study and in other recent literature (Table 1; Fig. 1; Guo et al., 2014, 2018; He et
387 al., 2013; Zhang, 2013; Zhong et al., 2014, 2015; Zou et al., 2008) were all the products of the same
388 tectonic-thermal event.

389 As discussed above, the mantle source of WNCC basalts have underwent metasomatism by melts
390 from subducted terrigenous sediments. The subduction of both Paleo-Asian oceanic slab and Mongolia-
391 Okhotsk seafloor slab could bring the sediments into mantle. However, given that the Tertiary basalt-
392 hosting mantle xenoliths from northern margin of NCC have the character of metasomatism by melts of
393 Paleo-Asian Ocean sediments (Wang et al., 2019) and the north margin of the WNCC is closed to the
394 Solonker suture spatially. We preferred that the Paleo-Asian Ocean subducted sediment is more prior to
395 affect the NCC lithospheric mantle.

396 Following this interpretation, we propose a petrogenic model for the WNCC basalts as follows.
397 In the Paleozoic, the Paleo-Asian oceanic slab subducted underneath the North China Craton (Li, 2006;
398 Xiao et al., 2003; Zhang et al., 2009), carrying continent-derived sediments (Fig. 10a). Melts derived
399 from these subducted sediments metasomatized the base of the lithosphere mantle beneath the northern

400 margin of the WNCC and formed the metasomatic veins (Wang et al., 2019; Fig. 10a). Such a
401 metasomatized mantle was subsequently overprinted by metasomatism of low-F melts that derived from
402 the asthenosphere/LVZ (Fig. 10a). The closure of the Paleo-Asian ocean was followed by the closure of
403 the Mongolia-Okhotsk Ocean and the formation of Central Asian Orogenic Belt (CAOB) during the
404 Jurassic to the earliest Cretaceous (Fig. 10b & c; Donskaya et al., 2013; Tomurtogoo et al., 2005). The
405 following breakoff of subducted Mongolia-Okhotsk seafloor slab led to the CAOB region and nearby
406 area in an extension background (Fig. 10d) as manifested by Cretaceous extensional basins and
407 metamorphic core complexes (Davis et al., 2002; Graham et al., 2001). Also for this reason, slab breakoff
408 induced asthenosphere upwelling could produce thermal perturbation at the base of the continental
409 lithosphere and heated the earlier formed metasomatized lithospheric mantle to facilitate the fusible
410 component melting, producing magmas parental to basalts in this study (Fig. 10d). This model explains
411 the widespread early Cretaceous magmatism that concentrated along the northern margin of the WNCC.

412 **6. Conclusion**

413 The widespread 107.3-133.1 Ma basaltic magmatism in the WNCC originated from partial
414 melting of the metasomatized lithospheric mantle. The mantle source of these basalts contains
415 amphibole/phlogopite, which were formed through metasomatism by low-F melts from asthenosphere
416 mantle and silicic melts derived from the subducted terrigenous sediments. The occurrence of
417 magmatism in WNCC was most probably related to the seafloor slab breakoff following the closure of
418 the Mongolia-Okhotsk ocean, in which scenario upwelling asthenosphere produced thermal perturbation
419 at the base of the lithosphere and heated the lithospheric mantle base, resulting in the melting of the early
420 metasomatized lithospheric mantle materials.

421 **Acknowledgments**

422 We are grateful to Meng Duan, Xiaohong Wang and Hongmei Gong for their assistance with bulk
423 rock major elements analysis, trace elements analysis and Sr-Nd-Hf isotopes compositions analysis,
424 respectively. P.Y. thank Shuo Chen and Huahua Cao for their helpful advice on the manuscript. And we
425 also thank two anonymous reviewers and the editor Xianhua Li for their constructive reviews. This work
426 was supported by the NSFC-Shandong Joint Fund for Marine Science Research Centers (U1606401),
427 the National Natural Science Foundation of China (NSFC Grants 41776067, 41630968, 91014003).

428 **Reference**

- 429 Abbott, D., Drury, R., Mooney, W., 1997. Continents as lithological icebergs: The importance of buoyant
430 lithospheric roots. *Earth and Planetary Science Letters* 149, 15-27.
- 431 Chen, S., Wang, X.H., Niu, Y.L., Sun, P., Duan, M., Xiao, Y.Y., Guo, P.Y., Gong, H.M., Wang, G.D., Xue,
432 Q.Q., 2017. Simple and cost-effective methods for precise analysis of trace element abundances in
433 geological materials with ICP-MS. *Science Bulletin* 62, 277-289.
- 434 Chen, L., Cheng, C., Wei, Z.G., 2009. Seismic evidence for significant lateral variations in lithospheric
435 thickness beneath the central and western North China Craton. *Earth and Planetary Science Letters*
436 286, 171-183.
- 437 Cheng, T., Nebel, O., Sossi, P.A., Wu, J., Siebel, W., Chen, F.K., Nebel-Jacobsen, Y.J., 2018. On the Sr-
438 Nd-Pb-Hf isotope code of enriched, Dupal-type sub-continental lithospheric mantle underneath
439 south-western China. *Chemical Geology* 489, 46-60.
- 440 Dai, L.Q., Zheng, Y.F., Zhao, Z.F., 2016. Termination time of peak decratonization in North China:
441 Geochemical evidence from mafic igneous rocks. *Lithos* 240-243, 327-336.
- 442 Davis, G., J. Darby, B., Zheng, Y.D., L. Spell, T., 2002. Geometric and temporal evolution of an
443 extensional detachment fault, Hohhot metamorphic core complex, Inner Mongolia, China. *Geology*
444 30, 1003-1006.
- 445 Deino, A., Potts, R., 1990. Single-crystal $^{40}\text{Ar}/^{39}\text{Ar}$ dating of the Olorgesailie Formation, Southern Kenya
446 Rift. *Journal of Geophysical Research Solid Earth* 95, 8453-8470.
- 447 Donskaya, T.V., Gladkochub, D.P., Mazukabzov, A.M., Ivanov, A.V., 2013. Late Paleozoic – Mesozoic
448 subduction-related magmatism at the southern margin of the Siberian continent and the 150 million-
449 year history of the Mongol-Okhotsk Ocean. *Journal of Asian Earth Sciences* 62, 79-97.
- 450 Förster, M.W., Prelević, D., Buhre, S., Mertz-Kraus, R., Foley, S.F., 2019. An experimental study of the
451 role of partial melts of sediments versus mantle melts in the sources of potassic magmatism. *Journal*
452 *of Asian Earth Sciences* 177, 76-88.
- 453 Gao, S., Luo, T.C., Zhang, B.R., Zhang, H.F., Han, Y.W., Zhao, Z.D., Hu, Y.K., 1998. Chemical
454 composition of the continental crust as revealed by studies in East China. *Geochimica et*
455 *Cosmochimica Acta* 62, 1959-1975.
- 456 Gao, S., Rudnick, R.L., Xu, W.L., Yuan, H.L., Liu, Y.S., Walker, R.J., Puchtel, I.S., Liu, X.M., Huang,

457 H., Wang, X.R., Yang, J., 2008. Recycling deep cratonic lithosphere and generation of intraplate
458 magmatism in the North China Craton. *Earth and Planetary Science Letters* 270, 41-53.

459 Gao, S., Rudnick, R.L., Yuan, H.L., Liu, X.M., Liu, Y.S., Xu, W.L., Ling, W.L., Ayers, J., Wang, X.C.,
460 Wang, Q.H., 2004. Recycling lower continental crust in the North China craton. *Nature* 432, 892-
461 897.

462 Graham, S.A., Hendrix, M.S., Johnson, C.L., Badamgarav, D., Badarch, G., Amory, J., Porter, M.,
463 Barsbold, R., Webb, L., Hacker, B.R., 2001. Sedimentary record and tectonic implications of
464 Mesozoic rifting in southeast Mongolia. *Geological Society of America Bulletin* 113, 1560-1579.

465 Guo, F., Fan, W.M., Wang, Y.J., Lin, G., 2003. Geochemistry of late mesozoic mafic magmatism in west
466 Shandong Province, eastern China: Characterizing the lost lithospheric mantle beneath the North
467 China Block. *Geochemical Journal* 37, 63-77.

468 Guo, J.T., Guo, F., Yan Wang, C., Li, C.W., 2013. Crustal recycling processes in generating the early
469 Cretaceous Fangcheng basalts, North China Craton: New constraints from mineral chemistry, oxygen
470 isotopes of olivine and whole-rock geochemistry. *Lithos* 170-171, 1-16.

471 Guo, P.Y., Niu, Y.L., Sun, P., Wang, X.H., Gong, H.M., Duan, M., Zhang, Y., Kong, J.J., Tian, L.Y., Wu,
472 S.G., 2018. The Early Cretaceous bimodal volcanic suite from the Yinshan Block, western North
473 China Craton: Origin, process and geological significance. *Journal of Asian Earth Sciences* 160, 348-
474 364.

475 Guo, P.Y., Niu, Y.L., Ye, L., Liu, J.J., Sun, P., Cui, H.X., Zhang, Y., Gao, J.P., Su, L., Zhao, J.X., Feng,
476 Y.X., 2014. Lithosphere thinning beneath west North China Craton: Evidence from geochemical and
477 Sr–Nd–Hf isotope compositions of Jining basalts. *Lithos* 202-203, 37-54.

478 Hawkesworth, C. J., Gallagher, K., Hergt, J. M., & McDermott, F. (1993). Mantle and slab contributions
479 in arc magmas. *Annual Review of Earth and Planetary Sciences*, 21(1), 175–204.

480 He, Y.K., Wu, T.R., Jin, X., 2013. $^{40}\text{Ar}/^{39}\text{Ar}$ Laser Probe Dating of Siziwangqi Shoshonite and Its
481 Geological Significance. *Geology and Exploration* 49, 1114-1122 (in Chinese with English abstract).

482 Hui, J., Cheng, H.Y., Zhang, J., Zhang, K.J., Qu, J.F., Zhang, B.H., 2020. Early Cretaceous continent
483 basalts in the Alxa Block, NW China: geochronology, geochemistry, and tectonic implications.
484 *International Geology Review*, 1-18.

485 Jordan, T., 1988. Structure and Formation of the Continental Tectosphere. *Journal of Petrology Special*

486 Volume, 11-37.

487 Kong, J.J., Niu, Y.L., Sun, P., Xiao, Y.Y., Guo, P.Y., Hong, D., Zhang, Y., Shao, F.L., Wang, X.H., Duan,
488 M., 2019. The origin and geodynamic significance of the Mesozoic dykes in eastern continental China.
489 *Lithos* 332-333, 328-339.

490 Le Bas, M., Maitre, L., L. Streckeisen, A., B. A, Z., 1986. A Chemical Classification of Volcanic Rocks
491 Based on the Total Alkali-Silica Diagram. *Journal of Petrology* 27, 745-750.

492 Le Maitre, R.W., Bateman, P., Dudek, A., Keller, J., Lameyre, J., Le Bas, M.J., Sabine, P.A., Schmid,
493 R., Sorensen, H., Streckeisen, A., Wooley, A.R., Zanettin, B., 1989. A Classification of igneous rocks
494 and glossary of terms. Oxford: Blackwell.

495 Li, J.Y., 2006. Permian geodynamic setting of Northeast China and adjacent regions: closure of the Paleo-
496 Asian Ocean and subduction of the Paleo-Pacific Plate. *Journal of Asian Earth Sciences* 26, 207-224.

497 Li, Y., Xu, W.L., Tang, J., Pei, F.P., Wang, F., Sun, C.Y., 2018. Geochronology and geochemistry of
498 Mesozoic intrusive rocks in the Xing'an Massif of NE China: Implications for the evolution and
499 spatial extent of the Mongol–Okhotsk tectonic regime. *Lithos* 304-307, 57-73.

500 Ling, W.L., Duan, R.C., Xie, X.J., Zhang, Y.Q., Zhang, J.B., Cheng, J.P., Liu, X.M., Yang, H.M., 2009.
501 Contrasting geochemistry of the Cretaceous volcanic suites in Shandong province and its implications
502 for the Mesozoic lower crust delamination in the eastern North China craton. *Lithos* 113, 640-658.

503 Liu, D.Y., Nutman, A.P., Compston, W., Wu, J.S., Shen, Q.H., 1992. Remnants of ≥ 3800 Ma crust in
504 the Chinese part of the Sino-Korean craton. *Geology* 20, 339-342.

505 Liu, Y.S., Gao, S., Kelemen, P.B., Xu, W.L., 2008. Recycled crust controls contrasting source
506 compositions of Mesozoic and Cenozoic basalts in the North China Craton. *Geochimica et*
507 *Cosmochimica Acta* 72, 2349-2376.

508 Liu, Y.S., Gao, S., Yuan, H.L., Zhou, L., Liu, X.M., Wang, X.C., Hu, Z.C., Wang, L.S., 2004. U–Pb
509 zircon ages and Nd, Sr, and Pb isotopes of lower crustal xenoliths from North China Craton: insights
510 on evolution of lower continental crust. *Chemical Geology* 211, 87-109.

511 Ma, L., Jiang, S.-Y., Hofmann, A.W., Dai, B.-Z., Hou, M.-L., Zhao, K.-D., Chen, L.-H., Li, J.-W., Jiang,
512 Y.-H., 2014. Lithospheric and asthenospheric sources of lamprophyres in the Jiaodong Peninsula: A
513 consequence of rapid lithospheric thinning beneath the North China Craton? *Geochimica et*
514 *Cosmochimica Acta* 124, 250-271.

515 Meng, F.X., Gao, S., Niu, Y.L., Liu, Y.S., Wang, X.R., 2015. Mesozoic–Cenozoic mantle evolution
516 beneath the North China Craton: A new perspective from Hf–Nd isotopes of basalts. *Gondwana*
517 *Research* 27, 1574-1585.

518 Niu, Y.L., O'Hara, M.J., 2003. Origin of ocean island basalts: A new perspective from petrology,
519 geochemistry, and mineral physics considerations. *Journal of Geophysical Research: Solid Earth* 108.

520 Niu, Y.L., 2008. The Origin of Alkaline Lavas. *Science* 320, 883-884.

521 Niu, Y.L., 2005. Generation and Evolution of Basaltic Magmas: Some Basic Concepts and a New View
522 on the Origin of Mesozoic- Cenozoic Basaltic Volcanism in Eastern China. *Geological Journal of*
523 *China Universities* 11, 9-46.

524 Niu, Y.L., Wilson, M., Humphreys, E.R., O'Hara, M.J., 2012. A trace element perspective on the source
525 of ocean island basalts (OIB) and fate of subducted ocean crust (SOC) and mantle lithosphere (SML).
526 *Episodes*. 35, 310-327.

527 Niu, Y.L., 2014. Geological understanding of plate tectonics: Basic concepts, illustrations, examples and
528 new perspectives. *Global Tectonics and Metallogeny* 10, 23-46.

529 Ouyang, H., Mao, J., Zhou, Z., Su, H., 2015. Late Mesozoic metallogeny and intracontinental magmatism,
530 southern Great Xing'an Range, northeastern China. *Gondwana Research* 27, 1153-1172.

531 Pilet, S., Baker, M.B., Stolper, E.M., 2008. Metasomatized Lithosphere and the Origin of Alkaline Lavas.
532 *Science* 320, 916-919.

533 Pilet, S., Baker, M.B., Müntener, O., Stolper, E.M., 2011. Monte Carlo Simulations of Metasomatic
534 Enrichment in the Lithosphere and Implications for the Source of Alkaline Basalts. *Journal of*
535 *Petrology* 52, 1415-1442.

536 Plank, T., Langmuir, C.H., 1998. The chemical composition of subducting sediment and its consequences
537 for the crust and mantle. *Chemical Geology* 145, 325-394.

538 Renne, P.R., Cassata, W.S., Morgan, L.E., 2009. The isotopic composition of atmospheric argon and
539 Ar/Ar geochronology: Time for a change? *Quaternary Geochronology* 4, 288-298.

540 Ringwood A E., 1975. *Composition and Petrology of the Earth's Mantle*. New York : McCraw-Hill , 618.

541 Sekine, T., Wyllie, P.J., 1983. Experimental Simulation of Mantle Hybridization in Subduction Zones.
542 *The Journal of Geology* 91, 511-528.

543 Shi, Y.N., Niu, F.L., Li, Z.H., Huangfu, P., 2020. Craton destruction links to the interaction between

544 subduction and mid-lithospheric discontinuity: Implications for the eastern North China Craton.
545 Gondwana Research 83, 49-62.

546 Soder, C., Altherr, R., Romer, R.L., 2016. Mantle Metasomatism at the Edge of a Retreating Subduction
547 Zone: Late Neogene Lamprophyres from the Island of Kos, Greece. *Journal of Petrology* 57, 1705-
548 1728.

549 Stracke, A., Bizimis, M., Salters, V.J.M., 2003. Recycling oceanic crust: Quantitative constraints.
550 *Geochemistry, Geophysics, Geosystems* 4, 1-33.

551 Stracke, A., Hofmann, A., Hart, S., 2005. FOZO, HIMU, and the rest of the mantle zoo. *Geochemistry,*
552 *Geophysics, Geosystems* 6(5), 1-20.

553 Sun, P., Niu, Y.L., Guo, P.Y., Chen, S., Duan, M., Gong, H.M., Wang, X.H., Xiao, Y.Y., 2019. Multiple
554 mantle metasomatism beneath the Leizhou Peninsula, South China: evidence from elemental and Sr-
555 Nd-Pb-Hf isotope geochemistry of the late Cenozoic volcanic rocks. *International Geology Review*
556 61, 1768-1785.

557 Sun, S.S., McDonough, W.F., 1989. Chemical and isotopic systematics of oceanic basalts: implications
558 for mantle composition and processes. Geological Society, London, Special Publications 42, 313-345.

559 Tiepolo, M., Bottazzi, P., Foley, S., Oberti, R., Vannucci, R., Zanetti, A., 2001. Fractionation of Nb and
560 Ta from Zr and Hf at mantle depths: the role of titanian pargasite and kaersutite. *Journal of Petrology*
561 42, 221-232.

562 Tomurtogoo, O., Windley, B.F., Kroner, A., Badarch, G., Liu, D.Y., 2005. Zircon age and occurrence of
563 the Adaatsag ophiolite and Muron shear zone, central Mongolia: constraints on the evolution of the
564 Mongol-Okhotsk ocean, suture and orogen. *Journal of the Geological Society* 162, 125-134.

565 Vasconcelos, P.N., Onoe, A.T., Kawashita, K., Soares, A.J., Teixeira, W., 2002. $^{40}\text{Ar}/^{39}\text{Ar}$ geochronology
566 at the Instituto de Geociencias, USP: instrumentation, analytical procedures, and calibration. *Anais*
567 *Da Academia Brasileira De Ciencias* 74, 297-342.

568 Vervoort, J.D., Blichert-Toft, J., 1999. Evolution of the depleted mantle: Hf isotope evidence from
569 juvenile rocks through time. *Geochimica et Cosmochimica Acta* 63, 533-556.

570 Wang, C.Y., Liu, Y.S., Foley, S.F., Zong, K.Q., Hu, Z.C., 2019. Lithospheric transformation of the
571 northern North China Craton by changing subduction style of the Paleo-Asian oceanic plate:
572 Constraints from peridotite and pyroxenite xenoliths in the Yangyuan basalts. *Lithos* 328-329, 58-68.

573 Wilde, S.A., 2015. Final amalgamation of the Central Asian Orogenic Belt in NE China: Paleo-Asian
574 Ocean closure versus Paleo-Pacific plate subduction — A review of the evidence. *Tectonophysics*
575 662, 345-362.

576 Workman, R.K., Hart, S.R., 2005. Major and trace element composition of the depleted MORB mantle
577 (DMM). *Earth and Planetary Science Letters* 231, 53-72.

578 Wu, F.Y., Walker, R.J., Yang, Y.H., Yuan, H.L., Yang, J.H., 2006. The chemical-temporal evolution of
579 lithospheric mantle underlying the North China Craton. *Geochimica et Cosmochimica Acta* 70, 5013-
580 5034.

581 Wu, F.Y., Xu, Y.G., Gao, S., Zheng, J.P., 2008. Lithospheric thinning and destruction of the North China
582 Craton. *Acta Petrologica Sinica* 24, 1145-1174 (in Chinese with English abstract).

583 Wyllie, P.J., Sekine, T., 1982. The formation of mantle phlogopite in subduction zone hybridization.
584 *Contributions to Mineralogy and Petrology* 79, 375-380.

585 Xiao, W.J., Windley, B., Hao, J.J., Zhai, M.G., 2003. Accretion leading to collision and the Permian
586 Solonker suture, Inner Mongolia, China: Termination of the Central Asian Orogenic Belt. *Tectonics*
587 22.

588 Xiong, X.L., Adam, J., Green, T.H., 2005. Rutile stability and rutile/melt HFSE partitioning during
589 partial melting of hydrous basalt: Implications for TTG genesis. *Chemical Geology* 218, 339-359.

590 Yang, D.B., Xu, W.L., Pei, F.P., Yang, C.H., Wang, Q.H., 2012. Spatial extent of the influence of the
591 deeply subducted South China Block on the southeastern North China Block: Constraints from Sr–
592 Nd–Pb isotopes in Mesozoic mafic igneous rocks. *Lithos* 136-139, 246-260.

593 Yang, Y.H., Zhang, H.F., Xie, L.W., Liu, Y., Qi, C.S., Tu, X.L., 2006. Petrogenesis of typical Mesozoic
594 and Cenozoic volcanic rocks from the North China Craton: new evidence from Hf isotopic studies.
595 *Acta Petrologica Sinica* 22, 1665-1671 (in Chinese with English abstract).

596 Zhang, H.F., Sun, M., Zhou, X.H., Fan, W.M., Zhai, M.G., Yin, J.F., 2002. Mesozoic lithosphere
597 destruction beneath the North China Craton: evidence from major-, trace-element and Sr–Nd–Pb
598 isotope studies of Fangcheng basalts. *Contributions to Mineralogy and Petrology* 144, 241-254.

599 Zhang, H.F., Sun, M., Zhou, X.H., Zhou, M.F., Fan, W.M., Zheng, J.P., 2003. Secular evolution of the
600 lithosphere beneath the eastern North China Craton: evidence from Mesozoic basalts and high-Mg
601 andesites. *Geochimica et Cosmochimica Acta* 67, 4373-4387.

602 Zhang, H.F., Sun, Y.L., Tang, Y.J., Xiao, Y., Zhang, W.H., Zhao, X.M., Santosh, M., Menzies, M.A.,
603 2012. Melt-peridotite interaction in the Pre-Cambrian mantle beneath the western North China Craton:
604 Petrology, geochemistry and Sr, Nd and Re isotopes. *Lithos* 149, 100-114.

605 Zhang, P.F., 2013. Geochemical characteristics and Petrogenesis of the Volcanic Rocks from the Middle
606 of the Yinshan Block. The University of Chinese Academy of Sciences.

607 Zhang, S.H., Zhao, Y., Song, B., Hu, J.M., Liu, S.W., Yang, Y.H., Chen, F.K., Liu, X.M., Liu, J., 2009.
608 Contrasting Late Carboniferous and Late Permian–Middle Triassic intrusive suites from the northern
609 margin of the North China craton: Geochronology, petrogenesis, and tectonic implications. *GSA*
610 *Bulletin* 121, 181-200.

611 Zhang, S.T., Wu, T.R., Xu, X., Byamba, J., Amarjargal, A., Wang, S.Q., Li, Z.Q., 2005. The Significance
612 of Discovery of Early Cretaceous Shoshonite in Central Inner Mongolia. *Acta Scientiarum Naturalium*
613 *Universitatis Pekinesis* 41, 212-218 (in Chinese with English abstract).

614 Zhao, G.C., Sun, M., Wilde, S.A., Li, S.Z., 2005. Late Archean to Paleoproterozoic evolution of the
615 North China Craton: key issues revisited. *Precambrian Research* 136, 177-202.

616 Zhao, G.C., Wilde, S.A., Cawood, P.A., Sun, M., Cruden, A.R., Easton, R.M., 2001. Archean blocks and
617 their boundaries in the North China Craton; lithological, geochemical, structural and P-T path
618 constraints and tectonic evolution. *Precambrian Research* 107, 45-73.

619 Zhao, Y., Zheng, J.P., Xiong, Q., Zhang, H., 2018. Destruction of the North China Craton triggered by
620 the Triassic Yangtze continental subduction/collision: A review. *Journal of Asian Earth Sciences* 164,
621 72-82.

622 Zhong, F.P., Zhong, J.H., Abdurahman, A., Wang, Y., You, W.F., Yang, W.L., 2015. Timing and scale of
623 the destruction of the North China craton: Revelation from the early cretaceous volcanic rocks in
624 Suhongtu Depression of Inggen-Ejin Banner Basin. *Geology in China* 42, 435-456 (in Chinese with
625 English abstract).

626 Zhong, F.P., Zhong, J.H., Wang, Y., Tian, W.F., 2014. Geochemistry Characteristics and Origin of Early
627 Cretaceous Volcanic Rocks in Suhongtu Depression, Inner Mongolia, China. *Acta Mineralogica*
628 *sinica* 34, 107-116 (in Chinese with English abstract).

629 Zhu, R.X., Chen, L., Wu, F.Y., Liu, J.L., 2011. Timing, scale and mechanism of the destruction of the
630 North China Craton. *Science China Earth Sciences* 54, 789-797.

- 631 Zhu, R.X., Pan, Y.X., He, H.Y., Qin, H.F., Ren, S.M., 2008. Palaeomagnetism and $^{40}\text{Ar}/^{39}\text{Ar}$ age from a
632 Cretaceous volcanic sequence, Inner Mongolia, China: Implications for the field variation during the
633 Cretaceous normal superchron. *Physics of the Earth and Planetary Interiors* 169, 59-75.
- 634 Zou, H.P., Zhang, K., Li, G., 2008. Cretaceous tectono-thermal event in the Ordos Block: an Ar-Ar
635 Chronological evidence from basalt at Hangjin banner, inner Mongolia, north China craton.
636 *Geotectonica et Metallogenia* 32, 360-364 (in Chinese with English abstract).
- 637

638 **Figure Captions**

639 **Fig. 1** (a) Sketch map of major tectonic divisions of the North China Craton (modified from Shi et al
640 (2020) and Zhao et al(2001)). Also shown are the early Cretaceous volcanism in the WNCC. (b) The
641 distribution and sample locations of the Wulate Zhongqi basalts.

642 **Fig. 2** Representative field photographs and petrography. (a) Volcanic rock outcrop in Wulate Zhongqi.
643 (b) Volcanic rock outcrop in Heishitougou. (c)-(f) Petrography of the basalts and andesitic basalts from
644 Wulate Zhongqi and Heishitougou. Pl- plagioclase; Mag- magnetite; Px- pyroxene; Ol- olivine.

645 **Fig. 3** Ar-Ar age spectra and $^{39}\text{Ar}/^{40}\text{Ar}$ vs. $^{36}\text{Ar}/^{40}\text{Ar}$ correlation of the whole rock sample ZQ14-47 from
646 Wulate Zhongqi.

647 **Fig. 4** MgO-variation diagrams showing major element oxides, $\text{CaO}/\text{Al}_2\text{O}_3$, Cr and Ni for basalts from
648 Wulate Zhongqi and Heishitougou. Arrows decreasing MgO approximate first-order trends dominated
649 by fractional crystallization. The arrows in the right represent the effect of fractional crystallization of
650 different minerals. Plag- plagioclase; Cpx- clinopyroxene; Ol- olivine.

651 **Fig. 5** Chondrite-normalized rare earth element and primitive mantle normalized incompatible element
652 patterns for basalts from Wulate Zhongqi and Heishitougou. Chondrite and primitive mantle values are
653 from Sun and McDonough (1989). For comparison, plotted also are average composition of present-day
654 oceanic island basalts (OIB; Sun and McDonough, 1989), global subducted sediment (GLOSS, Plank
655 and Langmuir, 1998), average crust of NCC (Gao et al., 1998) and the range of >110Ma Basalts from the
656 ENCC (Dai et al., 2016; Liu et al., 2008).

657 **Fig. 6** Sr, Nd and Hf isotope compositions of basalts from Wulate Zhongqi and Heishitougou. Plotted
658 also are the literature data of >110Ma Mesozoic basalts from the ENCC (Dai et al., 2016; Gao et al.,
659 2008; Guo et al., 2003; Guo et al., 2013; Ling et al., 2009; Meng et al., 2015; Yang et al., 2012; Yang et

660 al., 2006; Zhang et al., 2002, 2003), Early Cretaceous basalts from WNCC (Guo et al., 2014, 2018) and
661 Paleozoic kimberlite and mantle xenoliths (Wu et al., 2006 and references therein). Reference Terrestrial
662 Array ($\epsilon_{\text{Hf}}=1.36\epsilon_{\text{Nd}}+2.95$) is after Vervoort and Blichert-Toft (1999). Also shown are the present-day
663 compositions of oceanic island basalts (OIB) and mid-ocean ridge basalts (MORB) (Stracke et al., 2003;
664 Stracke et al., 2005). R value (correlation coefficient) of WNCC basalts was calculated excluding ZQ14-
665 29.

666 **Fig. 7** $\epsilon_{\text{Hf}}(t)$ vs. MgO/SiO₂ and Nb/La diagrams to show crustal materials contamination play negligible
667 role in the most WNCC basalts, except for ZQ14-09, ZQ14-26, ZQ14-52 and ZQ19-08.

668 **Fig. 8** (a) and (c) are P/Nd and Nb/La vs. $\epsilon_{\text{Nd}}(t)$ diagrams; (b) and (d) are P/Nd and Nb/La vs. $\epsilon_{\text{Hf}}(t)$ diagrams;
669 (e) Nb/La vs. Sm/Nd diagrams and (f) Nb/Th vs. Lu/Hf diagrams to show both the terrigenous sediments
670 and low-F melts contribution in the formation of the enriched mantle source of the WNCC basalts. We
671 select N-MORB (Sun and McDonough, 1989; Workman and Hart, 2005), represented by yellow star, as
672 the magma from partial melting of depleted mantle source and red star represents global subducted
673 sediment (GLOSS, Plank and Langmuir, 1998). The Double-headed arrows represent the variation trends
674 of the incompatible element ratios caused by the contribution of different metasomatism agents.

675 **Fig. 9** Trace element modelling of the multiple metasomatism melts in the mantle source region of the
676 basalts in Wulate Zhongqi and Heishitougou. We approximate basalts from Siziwangqi as the result of
677 partial melts derived from low-F melts metasomatized mantle (Guo et al., 2014) and choose global
678 subducted sediments (GLOSS, Plank and Langmuir, 1998) as the end-members of subducted terrigenous
679 sediments. The percentage in the figure (20%, 40%, 60%) means proportion of sediment.

680 **Fig. 10** Graphical description of the petrogenesis of the early Cretaceous basalts in the WNCC. (a) The
681 Paleo-Asian ocean slab subducted southward underneath the North China Craton in the late Paleozoic

682 and contributed terrigenous sediments into the mantle; and the silica-melts derived from the subducted
683 terrigenous sediments and low-F melts from asthenosphere metasomatized the overlying lithospheric
684 mantle, forming metasomatic veins at the base of the lithosphere; (b) The Paleo-Asian ocean was closed
685 in the early Mesozoic, leading to the orogenesis of the Central Asian Orogenic Belt (CAOB); (c) the
686 Mongolia-Okhotsk ocean closed in the Triassic to Middle Jurassic; (d) Breakoff of subducted Mongol-
687 Okhotsk oceanic slabs resulted in an upwelling of the asthenosphere, and such upwelling asthenosphere
688 produced thermal perturbation at the base of the lithosphere and heated the lithospheric mantle. The
689 fusible metasomatized components were, thus, melted and produced the primary magmas parental to
690 the basalts in this study. SLS in the figure indicated Solonker suture zone.

691 **Fig. S1** (a) The K_2O+Na_2O vs. SiO_2 diagram (Le Bas et al., 1986) and (b) K_2O vs. SiO_2 diagram (Le
692 Maitre et al., 1989) for basalts from Wulate Zhongqi and Heishitougou, for which, all the data plotted
693 have been normalized to 100% on a volatile-free basis.

694 **Fig. S2** Variation of selected trace element versus Zr for the Wulate Zhongqi and Heishitougou basalts.

695 R^2 is the square of correlation coefficients of Wulate Zhongqi Basalts.

696

697

Fig. 1

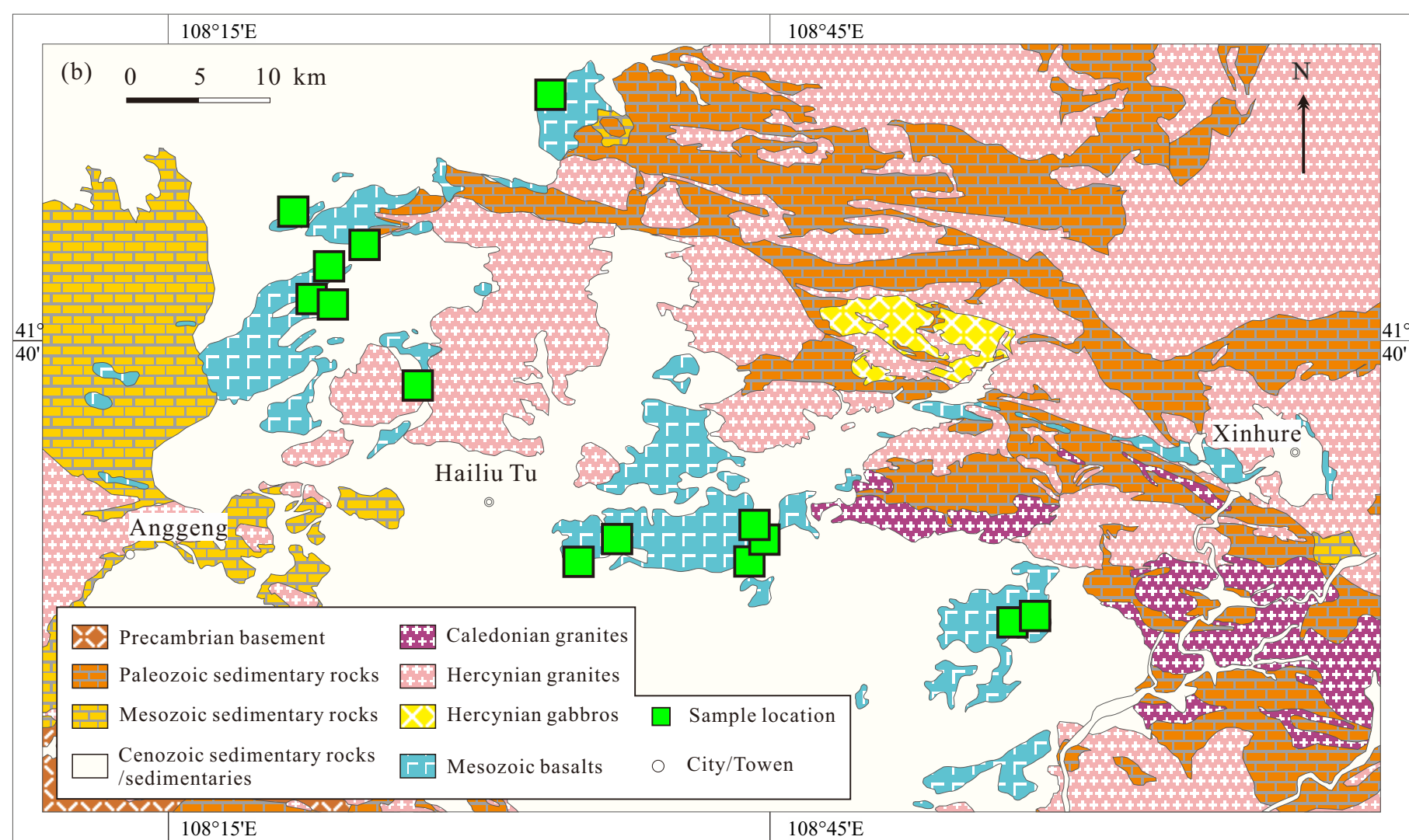
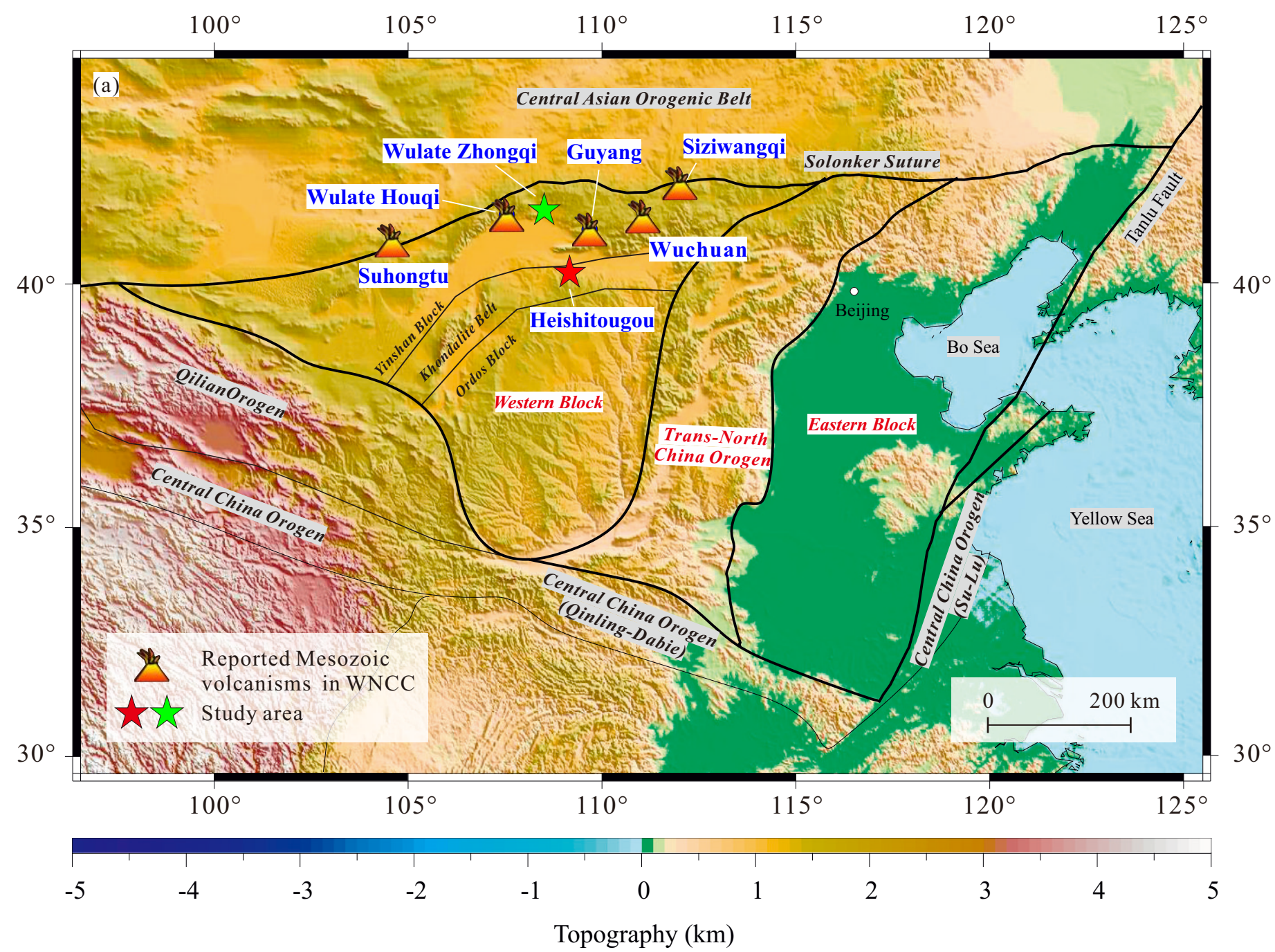


Fig. 2

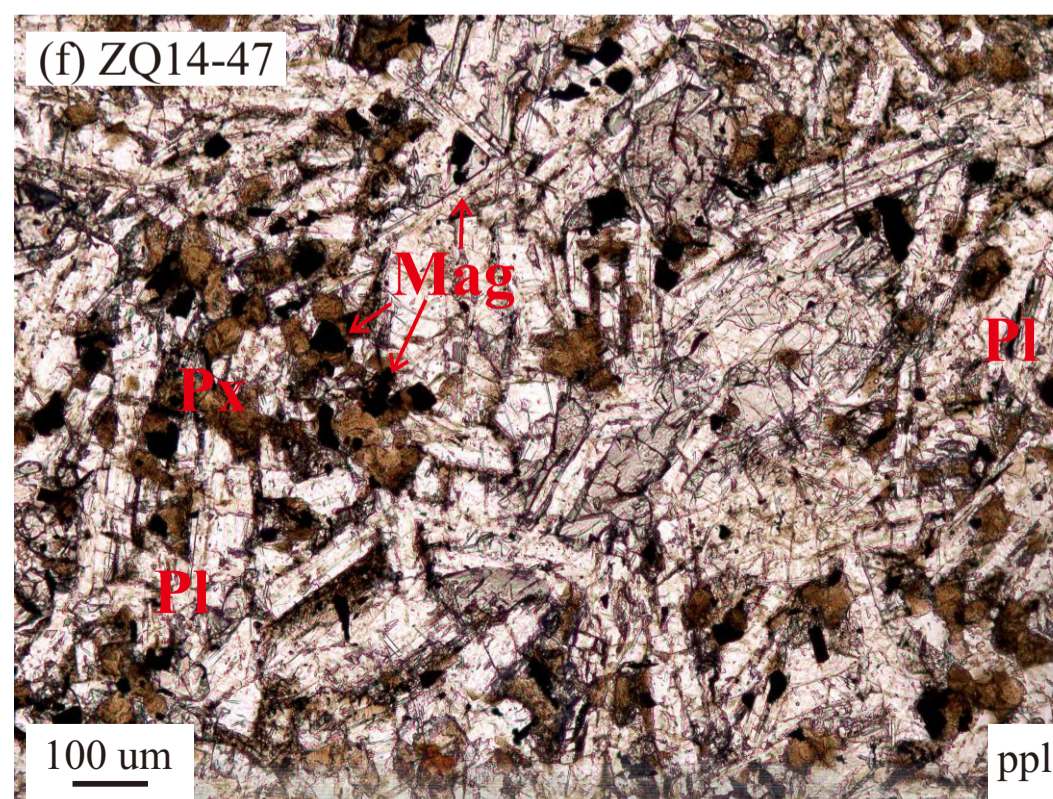
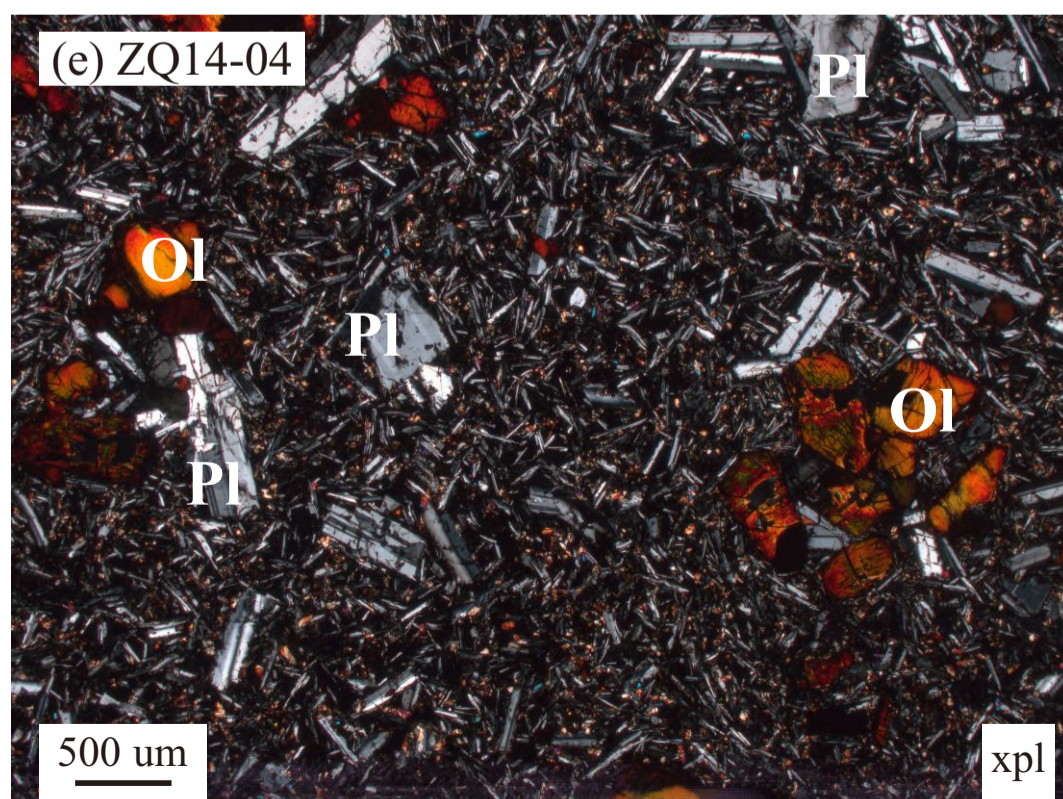
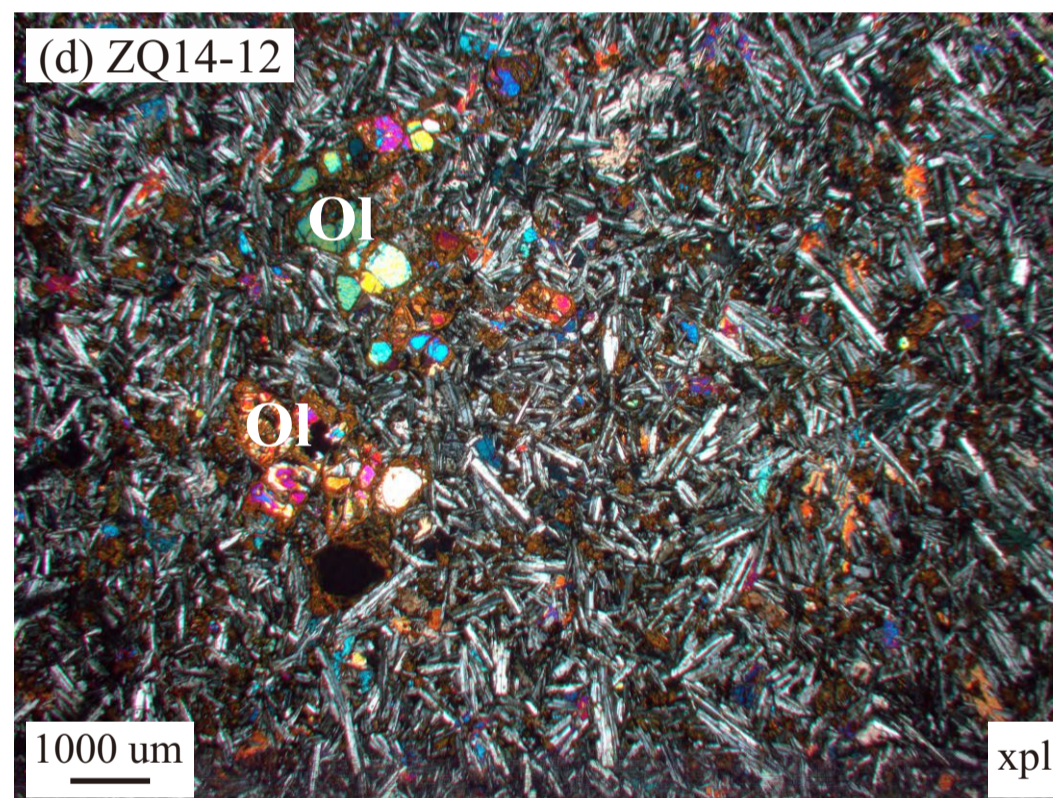
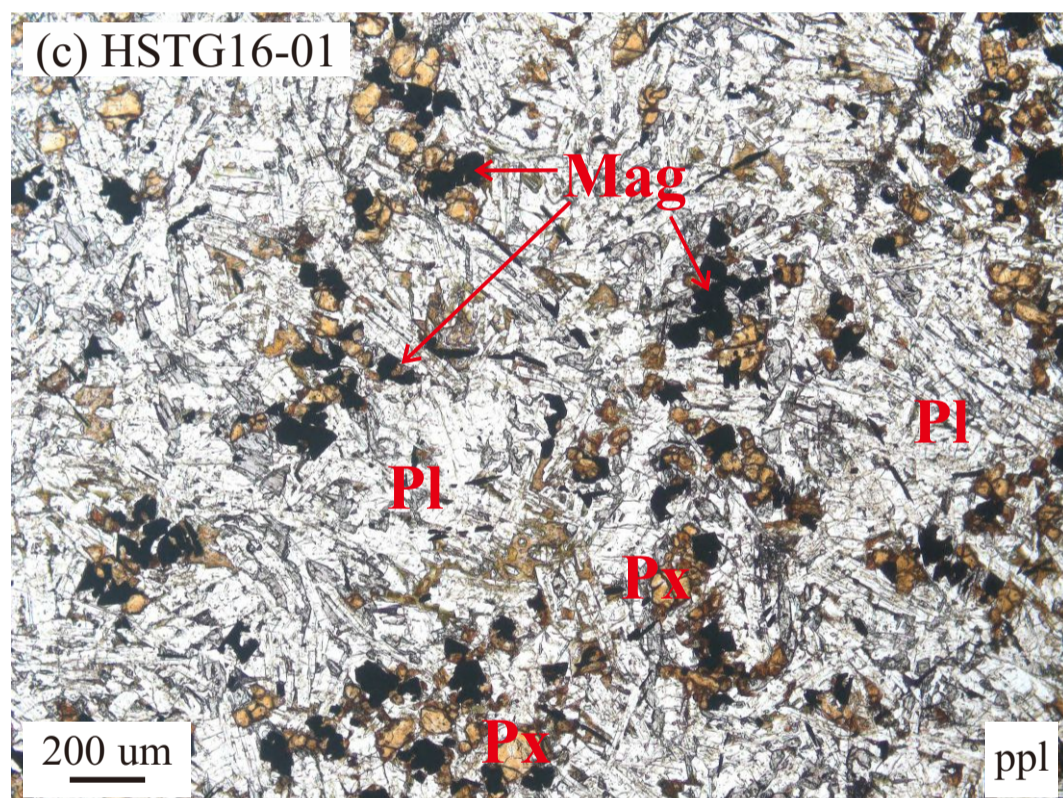
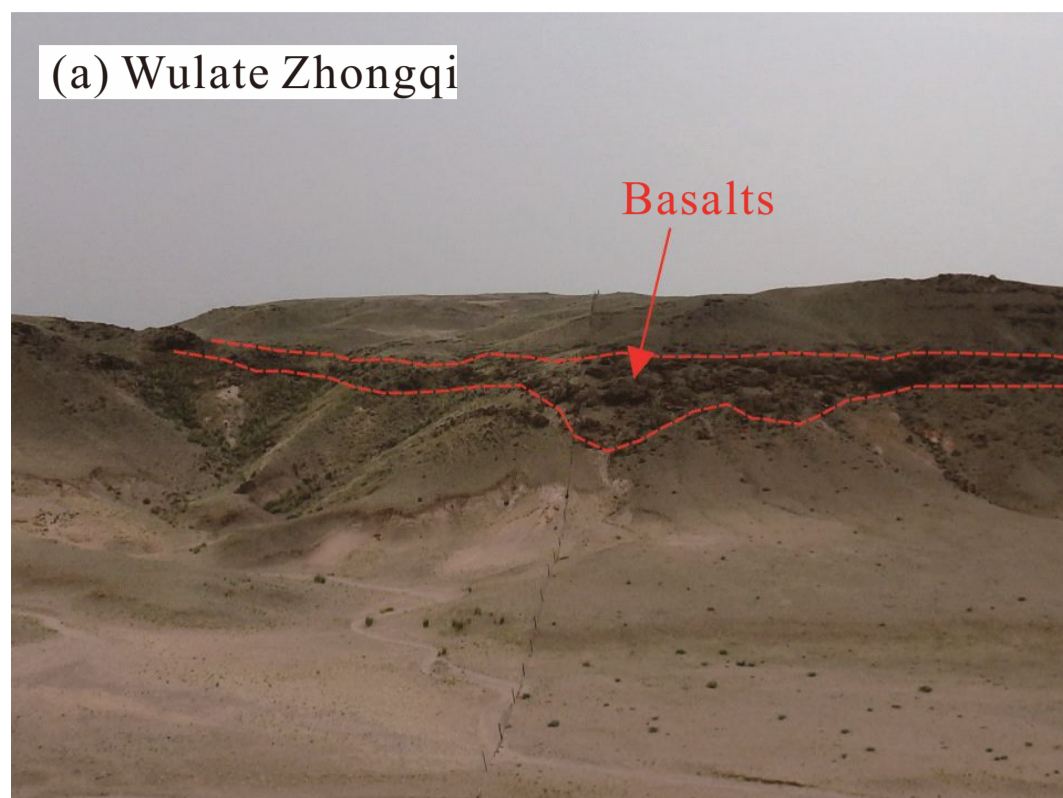


Fig. 3

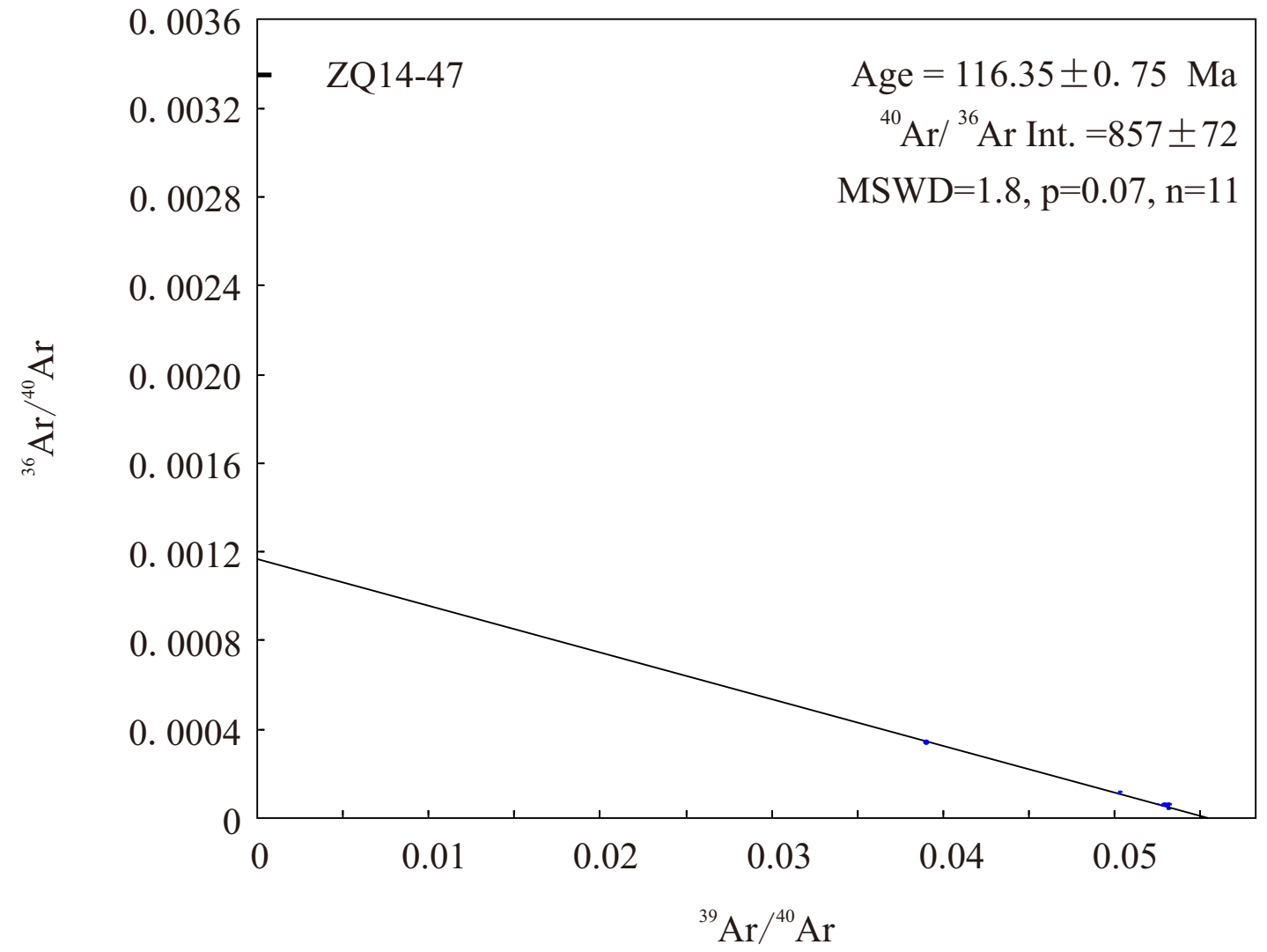
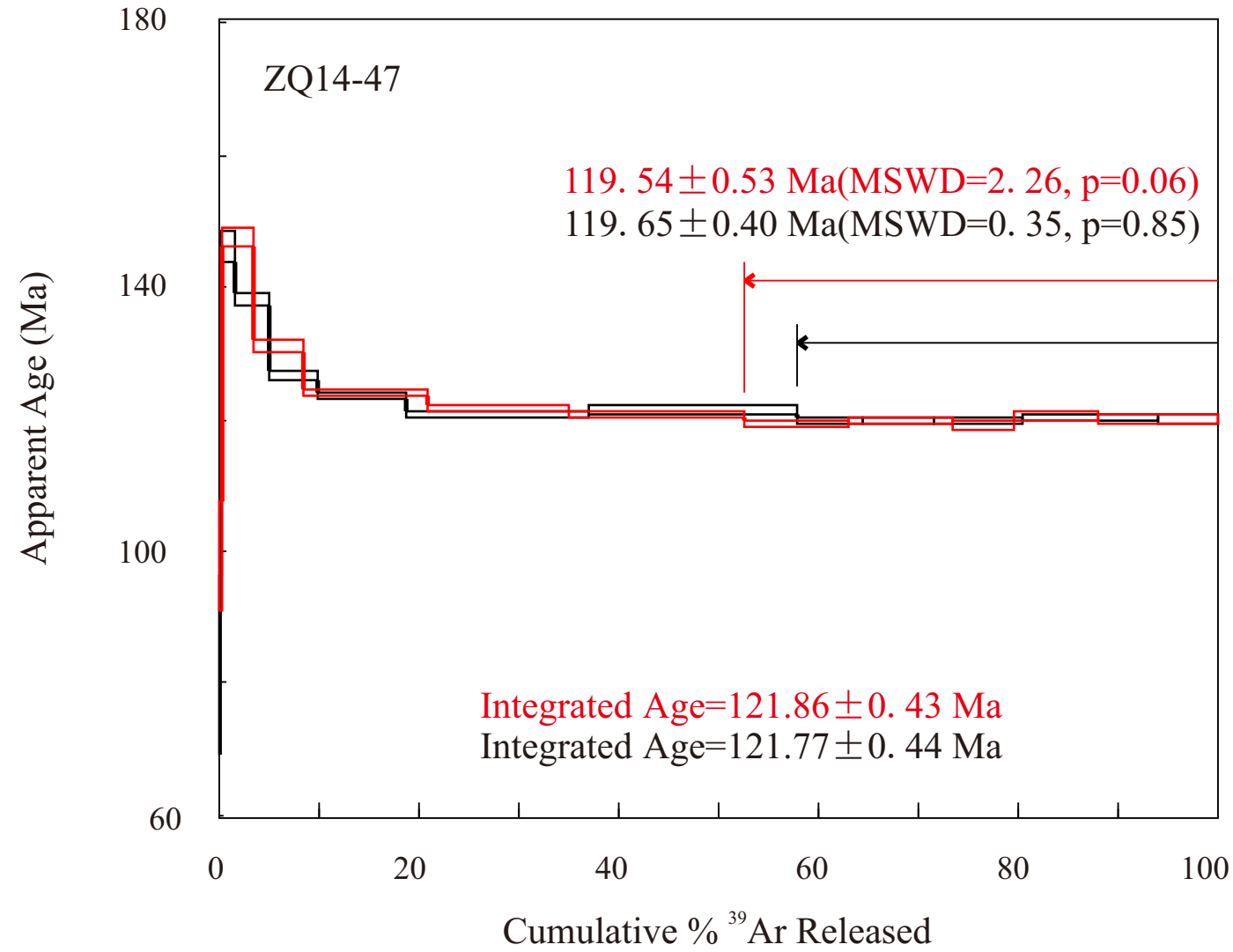


Fig. 4

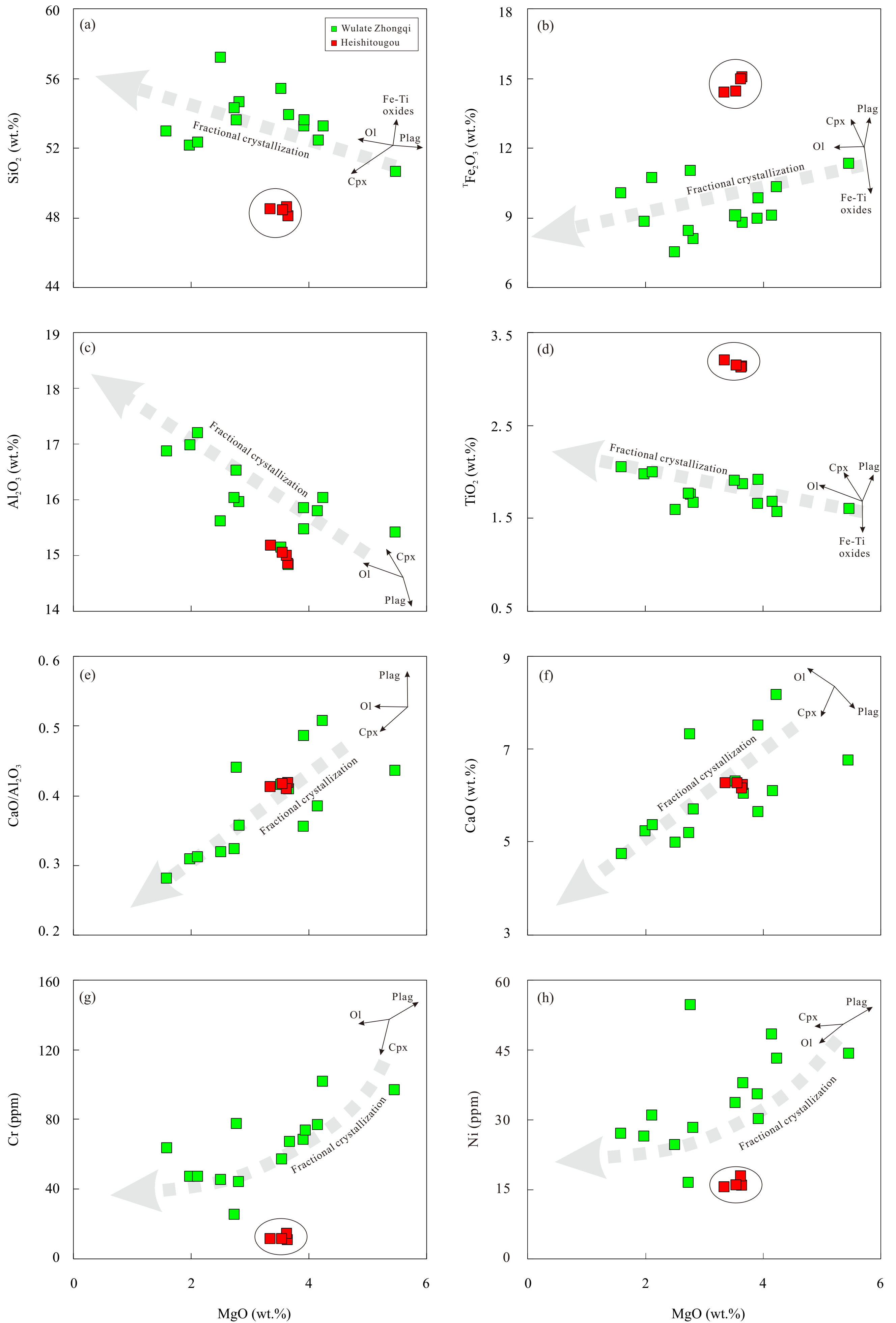


Fig.5

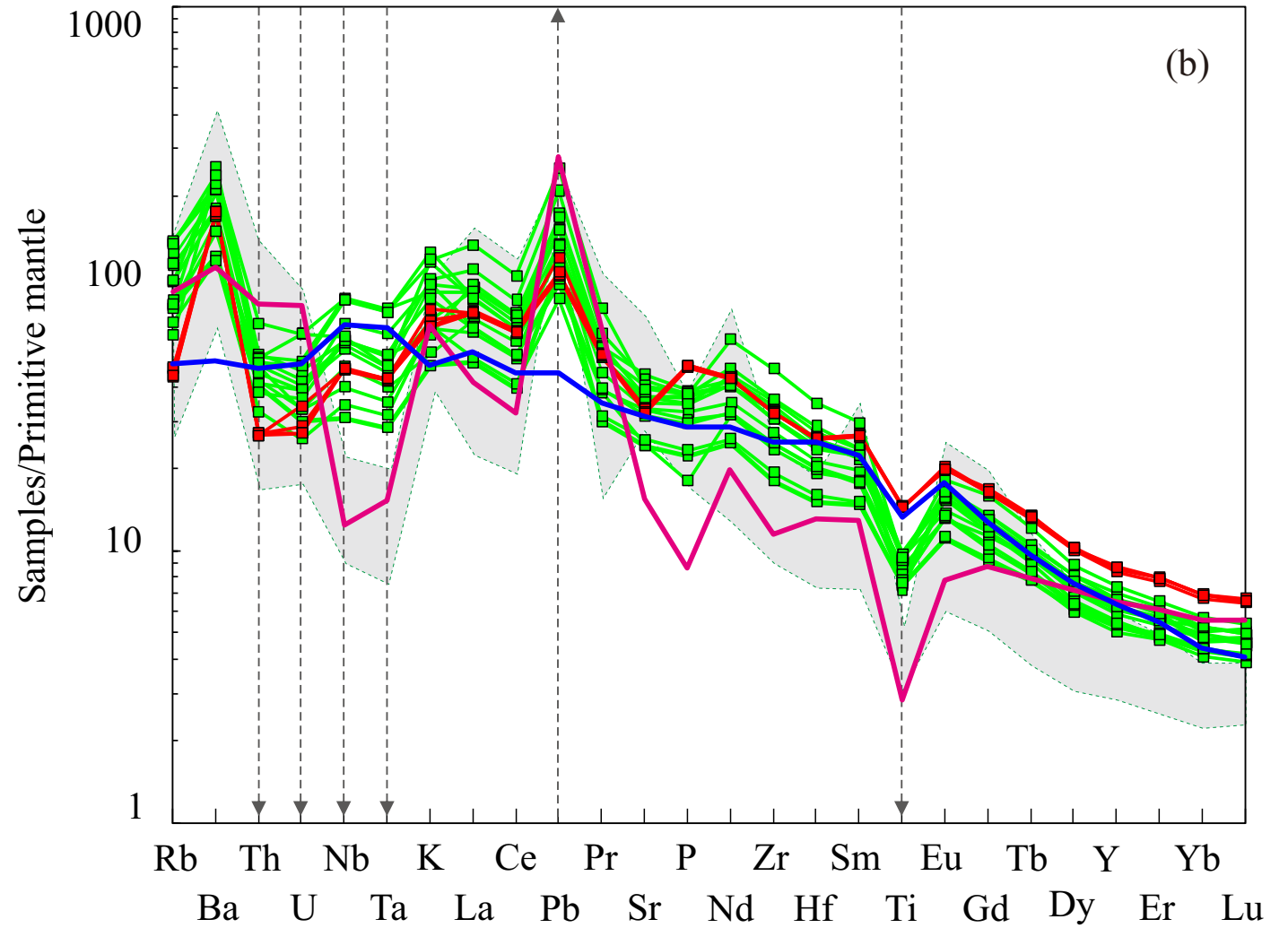
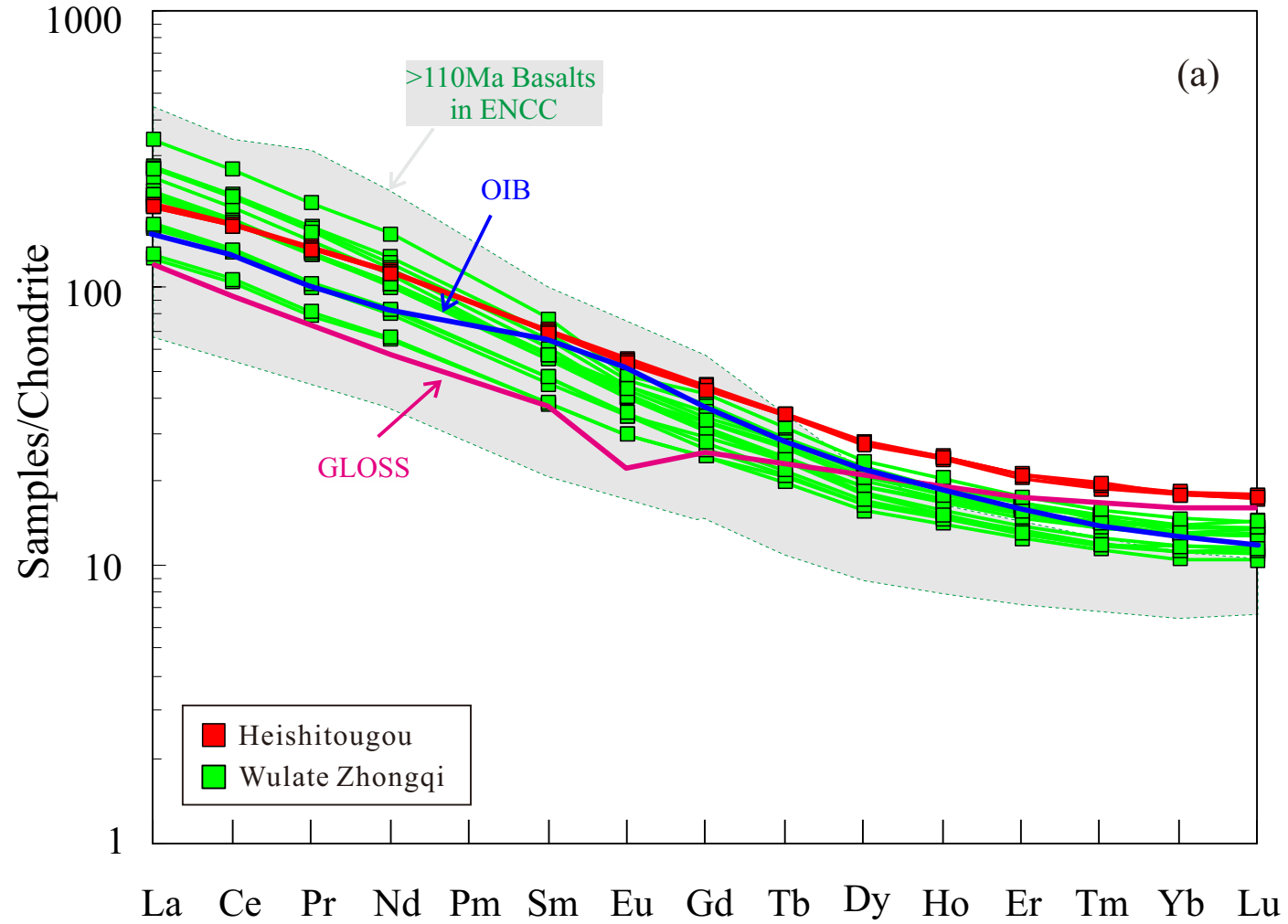


Fig. 6

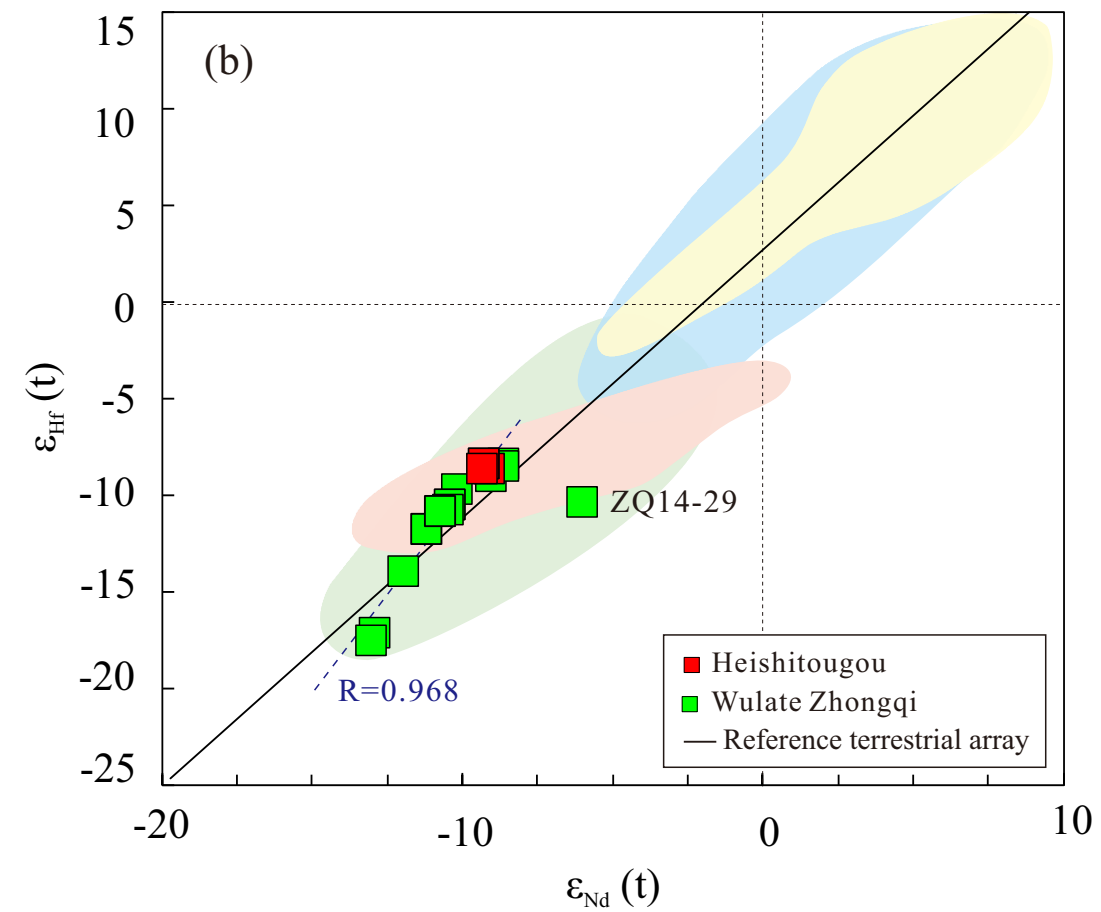
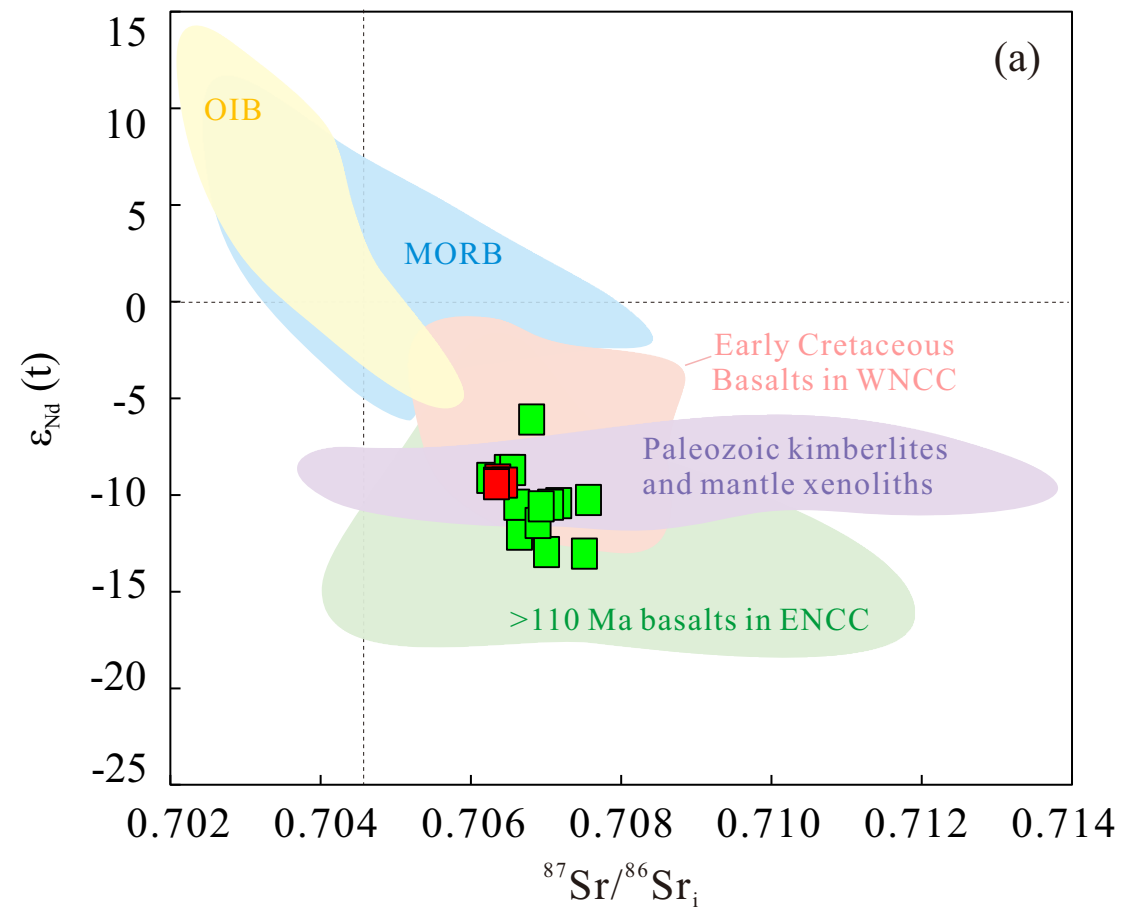


Fig.7

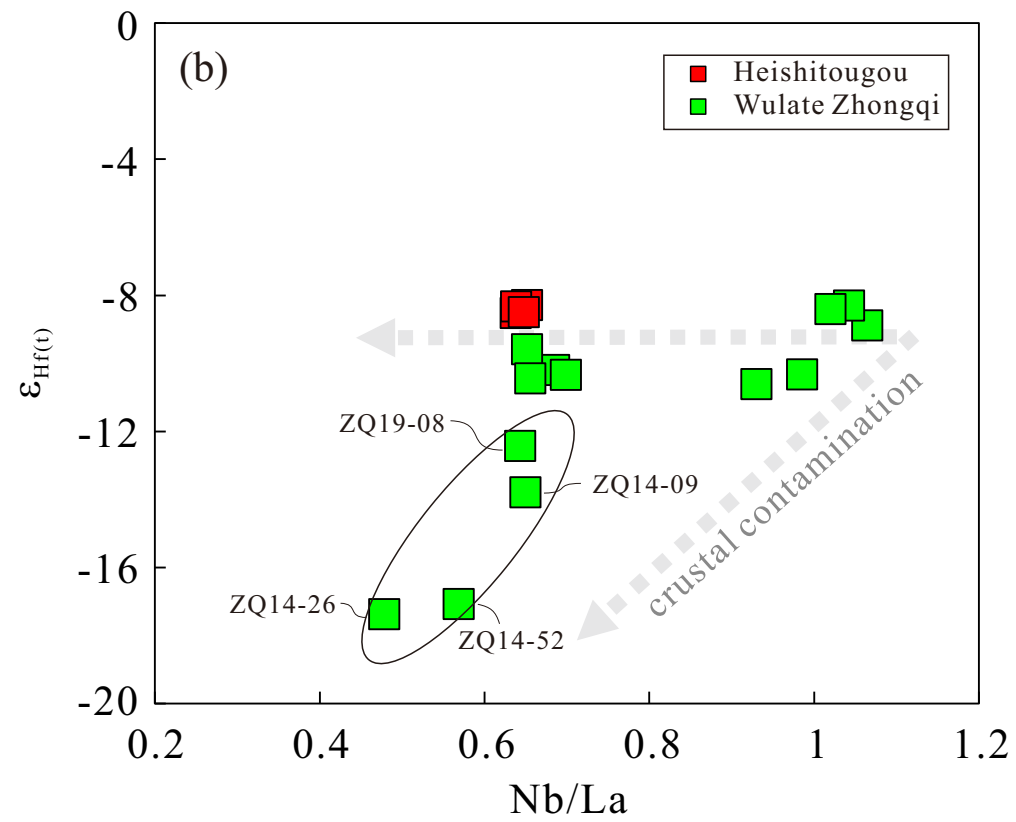
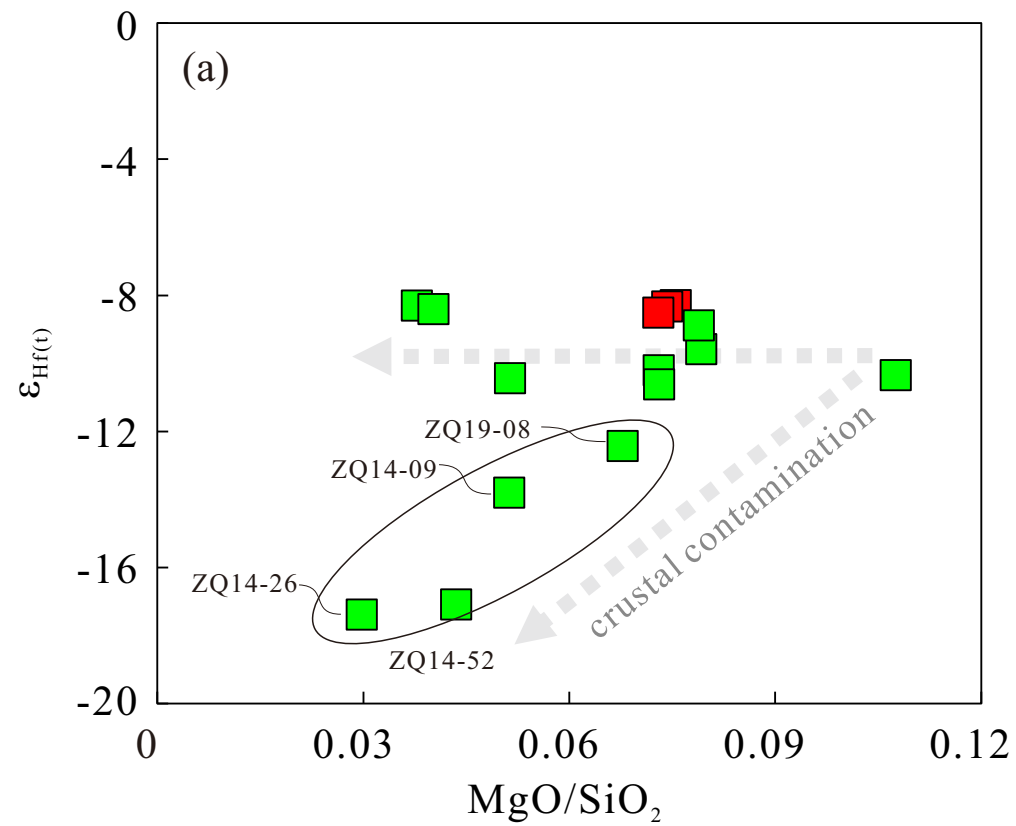


Fig.8

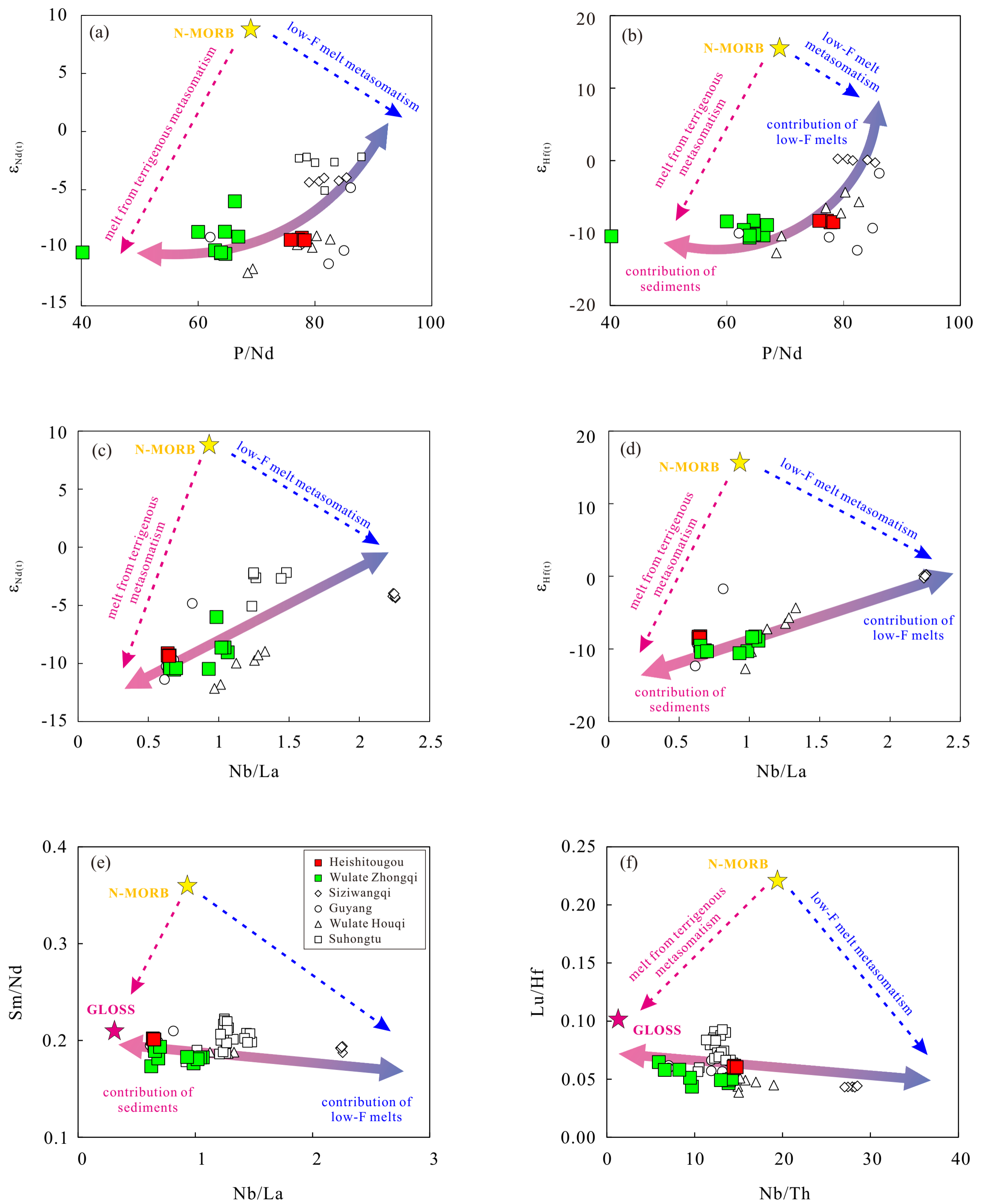


Fig. 9

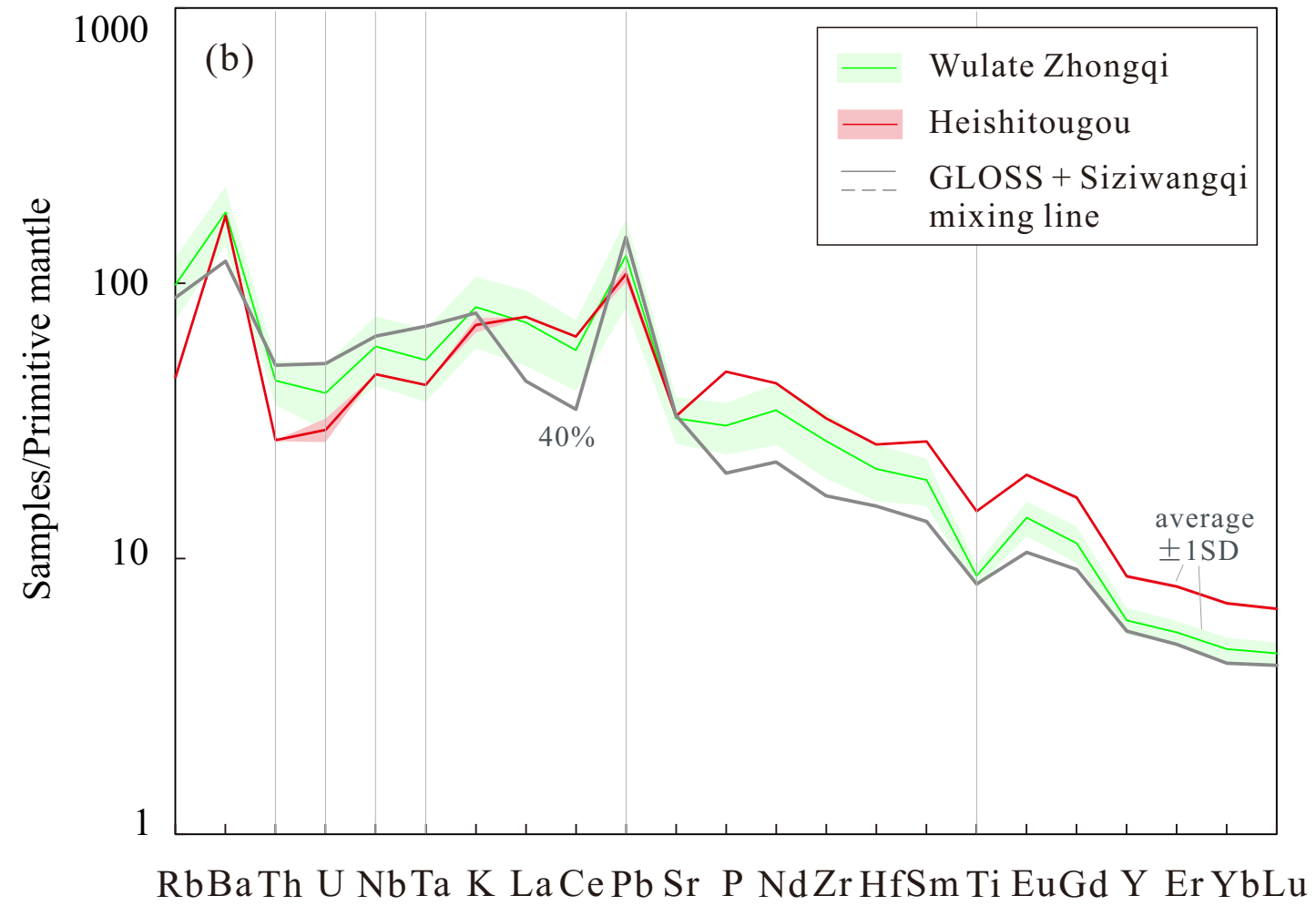
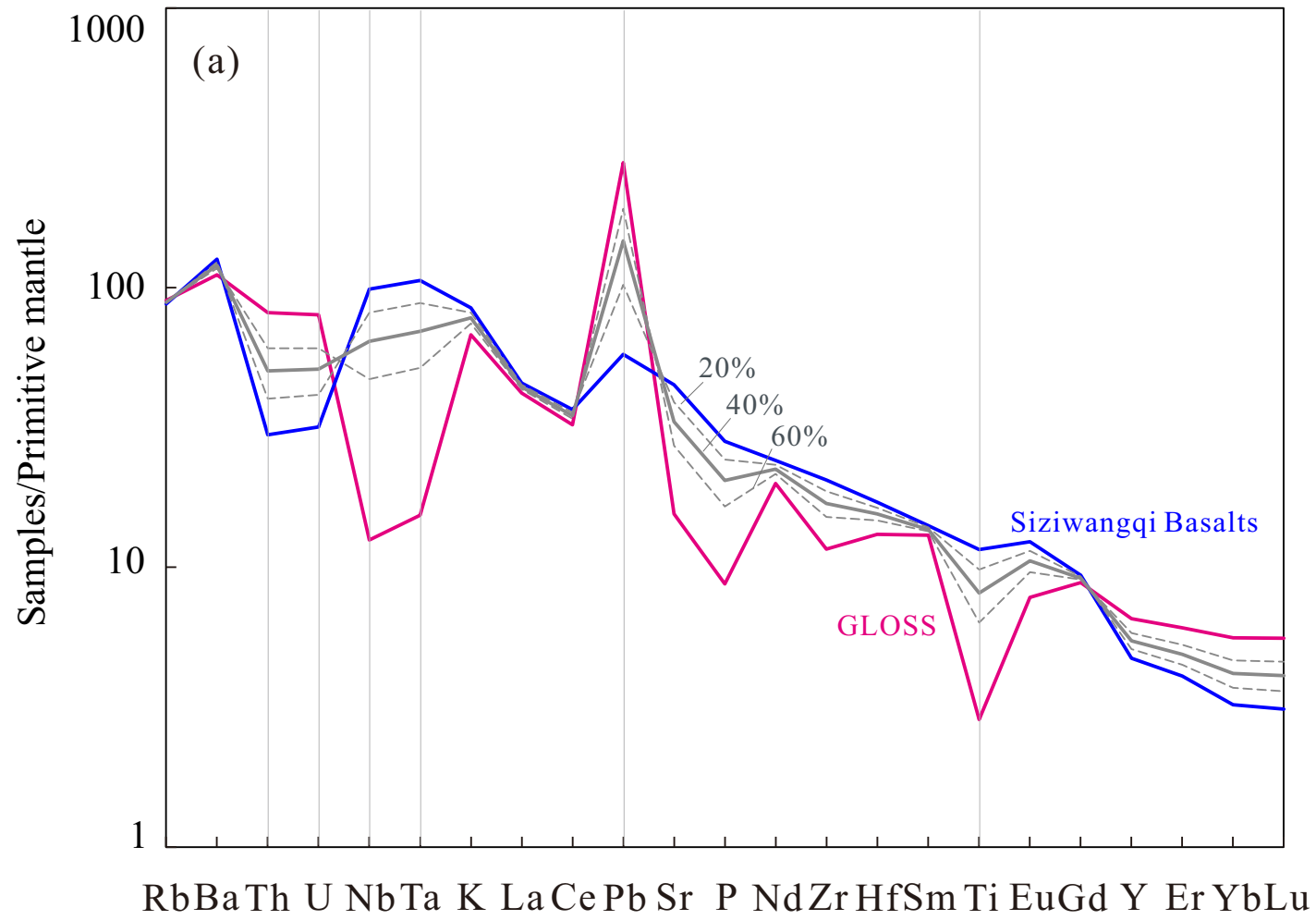
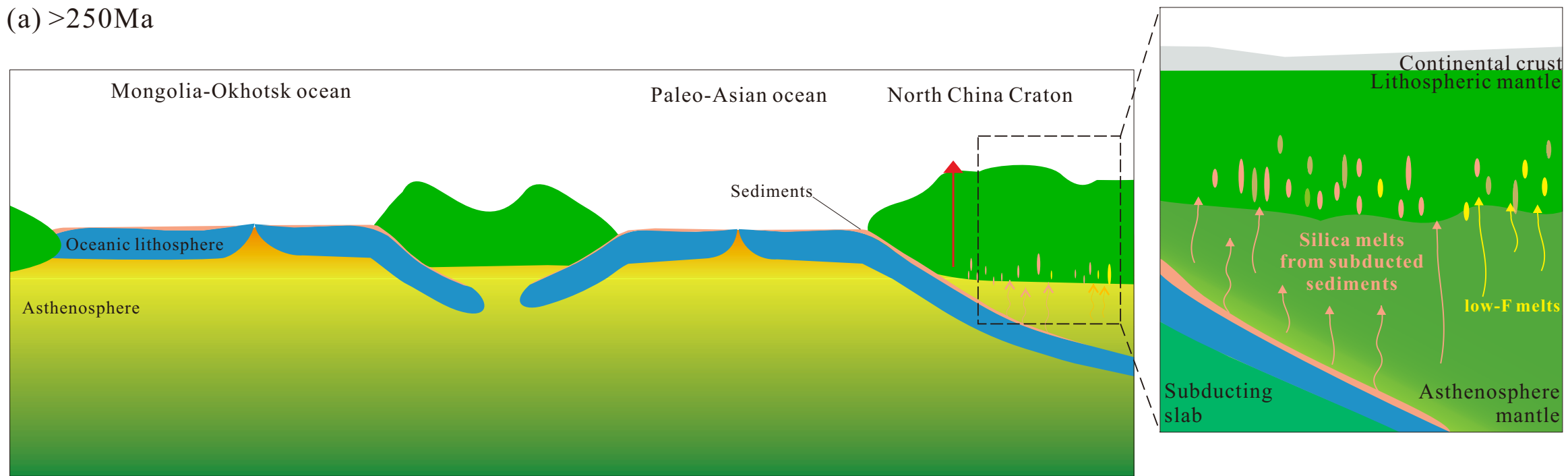
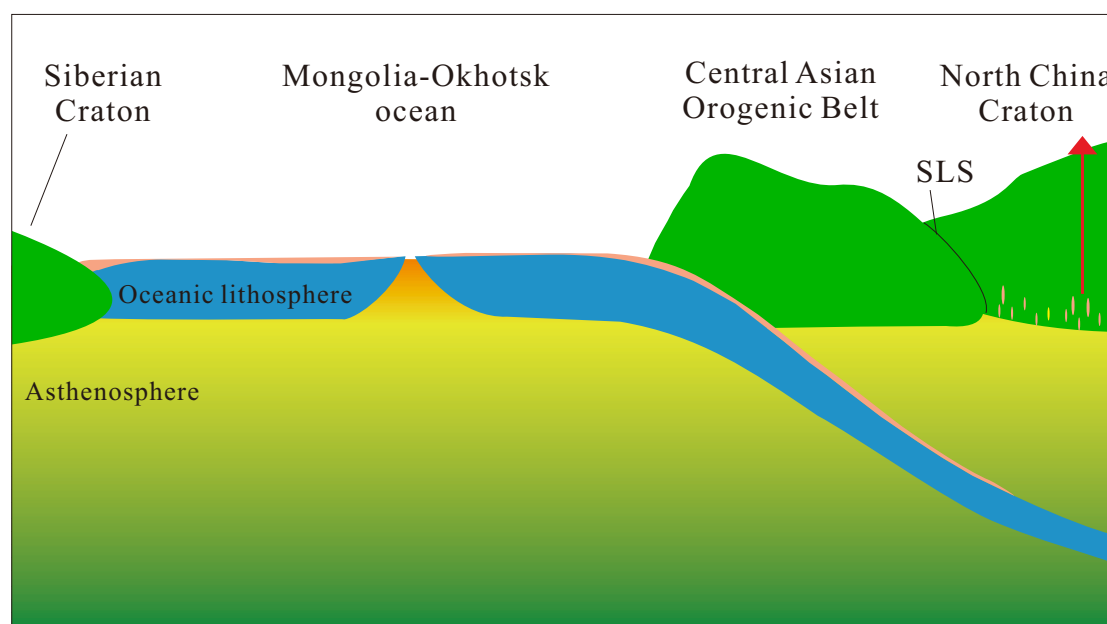


Fig. 10

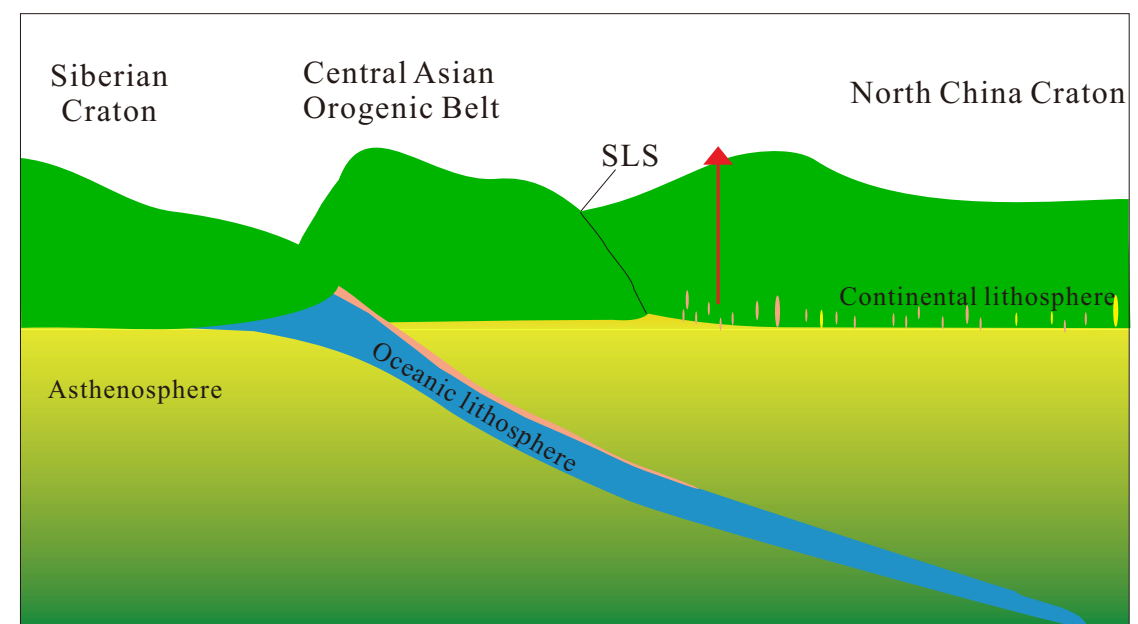
(a) >250Ma



(b) Triassic ~ Middle Jurassic



(c) Middle Jurassic



(d) ~120Ma

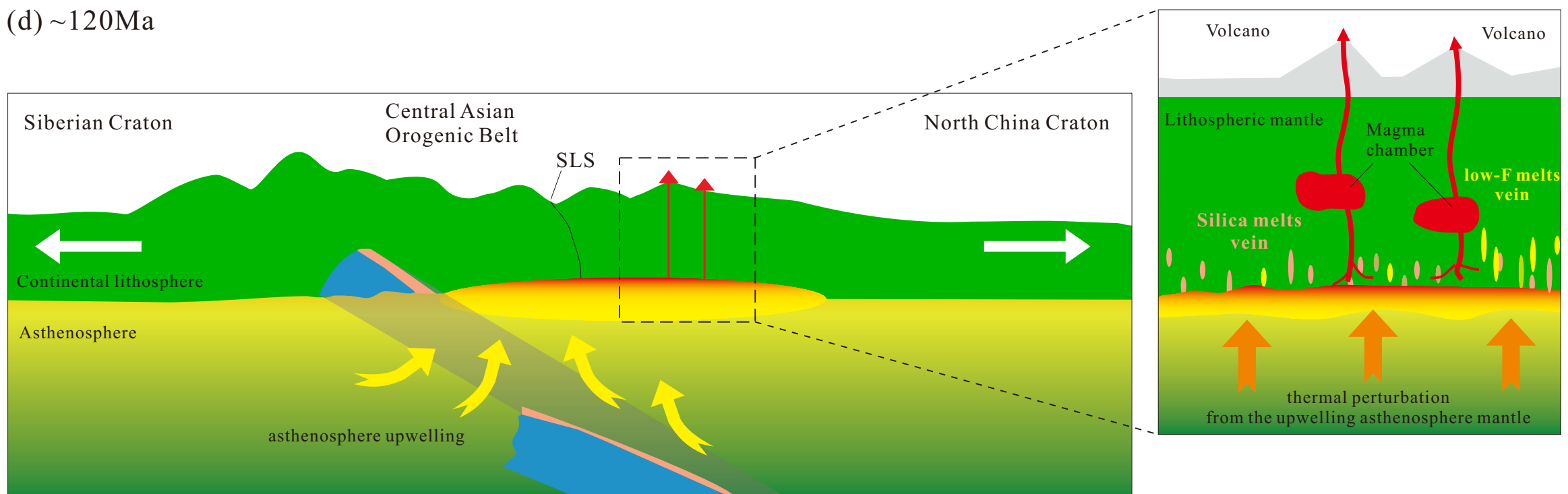


Table 1. Statistics of age data of early Cretaceous volcanics from the WNCC

Location	Rock type	Age (Ma)	Dating method	Data source	
Siziwang Qi	Shoshonite	127 ± 2	Whole rock Ar-Ar	He et al., 2013	
	Shoshonite	119.6 ± 1.4	Whole rock K-Ar	Zhang et al., 2005	
	Shoshonite	128.4 ± 1.8	Whole rock K-Ar		
	Shoshonite	108.6 ± 1.4	Whole rock K-Ar		
Guyang	Basalt	133.13 ± 0.91	Whole rock Ar-Ar	Guo et al., 2018	
	Basalt	123.47 ± 0.62	Whole rock Ar-Ar		
	Rhyolite	126.5 ± 1.3	SHRIMP zircon U-Pb		
	Rhyolite	126.1 ± 3.0	SHRIMP zircon U-Pb		
Wulate Zhongqi	Trachyte	122 ± 2	LA-ICP-MS Zircon U-Pb	Zhang, 2013	
	Rhyolite	135 ± 2	LA-ICP-MS Zircon U-Pb		
	Basalt	116.35 ± 0.75	Whole rock Ar-Ar	This study	
Wuchuan	Tuff	130 ± 3	LA-ICP-MS Zircon U-Pb	Zhang, 2013	
Heishitougou	Basalt	126.2 ± 0.4	Whole rock Ar-Ar	Zou et al., 2008	
Wulate Houqi	Basalt	114.42 ± 0.58	Whole rock Ar-Ar	Guo et al., 2018	
	Basalt	107.30 ± 0.54	Whole rock Ar-Ar		
Suhongtu	Andesite to basalt	114.1 ± 0.3	Whole rock Ar-Ar	Zhu et al., 2008	
	Andesite to basalt	113.8 ± 0.7	Whole rock Ar-Ar		
	Andesite to basalt	109.3 ± 2.8	Whole rock Ar-Ar		
	Andesite to basalt	110.8 ± 1.3	Whole rock Ar-Ar		
	Andesite to basalt	110.7 ± 1.6	Whole rock Ar-Ar		
	Andesite to basalt	110.3 ± 1.6	Whole rock Ar-Ar		
	Andesite to basalt	110.4 ± 1.2	Whole rock Ar-Ar		
	Andesite to basalt	110.9 ± 1.9	Whole rock Ar-Ar		
	Andesite to basalt	110.6 ± 1.5	Whole rock Ar-Ar		
	Andesite to basalt	111.1 ± 1.2	Whole rock Ar-Ar		
	Andesite to basalt	110.9 ± 2.3	Whole rock Ar-Ar		
	Alkali basalt	110.62 ± 1.40	Whole rock Ar-Ar		Zhong et al., 2015
	Alkali basalt	112.71 ± 2.06	Whole rock Ar-Ar		
	Alkali basalt	106.64 ± 1.38	Whole rock Ar-Ar		
Alkali basalt	106.48 ± 1.32	Whole rock Ar-Ar			
Alkali basalt	108.93 ± 1.68	Whole rock Ar-Ar			
Alkali basalt	109.51 ± 1.76	Whole rock Ar-Ar			

Table 2. Bulk rock Sr-Nd-Hf isotope analysis result for the early Cretaceous basalts from Wulate Zhongqi and Heishitougou and the USGS standard materials

Sample	$^{87}\text{Rb}/^{86}\text{Sr}$ ^a	$^{87}\text{Sr}/^{86}\text{Sr}\pm 1\sigma$	$^{87}\text{Sr}/^{86}\text{Sr}_i$ ^b	$^{147}\text{Sm}/^{144}\text{Nd}$ ^a	$^{143}\text{Nd}/^{144}\text{Nd}\pm 1\sigma$	$^{143}\text{Nd}/^{144}\text{Nd}_i$ ^b	$^{176}\text{Lu}/^{177}\text{Hf}$ ^a	$^{176}\text{Hf}/^{177}\text{Hf}\pm 1\sigma$	$^{176}\text{Hf}/^{177}\text{Hf}_i$ ^b	$\epsilon_{\text{Nd}(t)}$ ^c	$\epsilon_{\text{Hf}(t)}$ ^c
ZQ14-04	0.284658	0.708013±8	0.707543	0.116999	0.512054±2	0.511965	0.009202	0.282452±4	0.282431	-10.22	-9.58
ZQ14-06	0.278009	0.707603±7	0.707143	0.113846	0.512042±4	0.511955	0.008238	0.282425±2	0.282407	-10.40	-10.44
ZQ14-09	0.191951	0.706930±3	0.706613	0.101585	0.511952±6	0.511875	0.005541	0.282325±1	0.282312	-11.97	-13.79
ZQ14-12	0.236677	0.707432±6	0.707040	0.116473	0.512043±3	0.511955	0.008261	0.282428±2	0.282410	-10.41	-10.34
ZQ14-26	0.164826	0.707251±5	0.706978	0.100089	0.511901±3	0.511825	0.005393	0.282231±1	0.282220	-12.94	-17.08
ZQ14-29	0.132837	0.707000±6	0.706780	0.106168	0.512261±6	0.512180	0.006623	0.282425±2	0.282410	-6.01	-10.33
ZQ14-37	0.300084	0.706725±4	0.706229	0.109955	0.512109±2	0.512025	0.007035	0.282466±1	0.282451	-9.04	-8.89
ZQ14-40	0.322481	0.706985±4	0.706452	0.109773	0.512130±2	0.512046	0.006978	0.282483±1	0.282468	-8.62	-8.30
ZQ14-44	0.341646	0.707099±5	0.706534	0.108778	0.512128±2	0.512045	0.007145	0.282480±1	0.282465	-8.64	-8.41
ZQ14-47	0.273976	0.707038±7	0.706585	0.110126	0.512036±3	0.511952	0.006982	0.282417±1	0.282402	-10.47	-10.62
ZQ14-52	0.299392	0.707984±5	0.707488	0.097399	0.511895±2	0.511821	0.005268	0.282223±2	0.282211	-13.02	-17.38
ZQ19-08	0.265713	0.707303±6	0.706864	0.105005	0.511984±2	0.511904	0.006247	0.282364±2	0.282351	-11.40	-12.43
ZQ19-12	0.218088	0.707262±5	0.706901	0.109203	0.512032±3	0.511948	0.007274	0.282430±2	0.282414	-10.53	-10.20
HSTG16-01	0.122298	0.706551±6	0.706331	0.121700	0.512108±4	0.512008	0.008737	0.282490±3	0.282455	-9.13	-8.53
HSTG16-02	0.123237	0.706641±8	0.706420	0.121044	0.512099±5	0.511999	0.008463	0.282482±3	0.282462	-9.31	-8.29
HSTG16-04	0.117542	0.706525±8	0.706314	0.121502	0.512098±4	0.511998	0.008607	0.282481±3	0.282461	-9.33	-8.33
HSTG16-09	0.119337	0.706525±8	0.706310	0.121104	0.512096±4	0.511996	0.008571	0.282476±3	0.282456	-9.35	-8.50
BHVO-2		0.703524±4			0.513012±3			0.283085±1			
BCR-2		0.705113±5			0.512655±4			0.282859±2			
AGV-2		0.704016±5			0.512797±4			0.282979±3			

a. $^{87}\text{Rb}/^{86}\text{Sr}$, $^{147}\text{Sm}/^{144}\text{Nd}$ and $^{176}\text{Lu}/^{177}\text{Hf}$ are calculated using whole-rock Rb, Sr, Sm, Nd, Lu and Hf contents in Supplementary Table 1.

b. $^{87}\text{Sr}/^{86}\text{Sr}_i = [(^{87}\text{Sr}/^{86}\text{Sr}) - (^{87}\text{Rb}/^{86}\text{Sr})(e^{\lambda t} - 1)]$; $^{143}\text{Nd}/^{144}\text{Nd}_i = [(^{143}\text{Nd}/^{144}\text{Nd}) - (^{147}\text{Sm}/^{144}\text{Nd})(e^{\lambda t} - 1)]$; $^{176}\text{Hf}/^{177}\text{Hf}_i = [(^{176}\text{Hf}/^{177}\text{Hf}) - (^{176}\text{Lu}/^{177}\text{Hf})(e^{\lambda t} - 1)]$.

c. $\epsilon_{\text{Nd}(t)} = [(^{143}\text{Nd}/^{144}\text{Nd}_i)/(^{143}\text{Nd}/^{144}\text{Nd}_{\text{CHUR}}) - 1] \times 10000$, $^{143}\text{Nd}/^{144}\text{Nd}_{\text{CHUR}} = 0.512638$; $\epsilon_{\text{Hf}(t)} = [(^{176}\text{Hf}/^{177}\text{Hf}_i)/(^{176}\text{Hf}/^{177}\text{Hf}_{\text{CHUR}}) - 1] \times 10000$; $^{176}\text{Hf}/^{177}\text{Hf}_{\text{CHUR}} = 0.282772$.



Click here to access/download

**Supplementary material/Appendix (Files for online
publication only)**

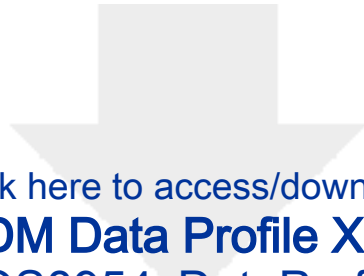
Supplementary Figures.pdf



[Click here to access/download](#)

Supplementary Interactive Plot Data (CSV)
Supplementary Tables.xlsx





Click here to access/download
RDM Data Profile XML
LITHOS8954_DataProfile.xml

